ABSTRACT

Title of Dissertation:	THE PHYSICS OF HIGH-INTENSITY LASER-MATTER INTERACTIONS AND APPLICATIONS
	Joshua J Isaacs Doctor of Philosophy, 2019
Dissertation directed by:	Professor Phillip Sprangle, Department of Physics and Department of Electrical and Computer Engineering and the Institute for Research in Electronics and Applied Physics

This dissertation consists of three separate research topics:

First, the effect of laser noise on the propagation of high-power and high-intensity short pulse lasers in dispersive and nonlinear media is studied. We consider the coupling of laser intensity noise and phase noise to the spatial and temporal evolution of laser radiation. We show that laser noise can have important effects on the propagation of high-power as well as high-intensity lasers in a dispersive and nonlinear medium such as air. We present atmospheric propagation examples of the spatial and temporal evolution of intensity and frequency fluctuations due to noise for laser wavelengths of $0.85 \ \mu m$, $1 \ \mu m$, and $10.6 \ \mu m$.

Next, a concept for all-optical remote detection of radioactive materials is presented and analyzed. The presence of excess radioactivity increases the level of

negative ions in the surrounding air region. This can act as a source of seed electrons for a laser-induced avalanche ionization breakdown process. We model irradiated air to estimate the density of negative ions and use a set of coupled rate equations to simulate a subsequent laser-induced avalanche ionization. We find that ion-seeded avalanche breakdown can be a viable signature for the detection of radioactivity, a conclusion which has been experimentally tested and verified.

Finally, we propose and analyze a mechanism to accelerate protons from close to rest in a laser-excited plasma wave. The beating of two counter-propagating laser pulses in a plasma shock-excites a slow forward-propagating wakefield. The trapping and acceleration of protons is accomplished by tapering both the plasma density and the amplitude of the backward-propagating pulse. We present an example in which protons are accelerated from 10 keV to 10 MeV in a distance of approximately 1 cm.

THE PHYSICS OF HIGH-INTENSITY LASER-MATTER INTERACTIONS
AND
APPLICATIONS

by

Joshua J Isaacs

Dissertation submitted to the Faculty of the Graduate School of the
University of Maryland, College Park, in partial fulfillment
of the requirements for the degree of
Doctor of Philosophy in
Physics
2019

Advisory Committee:
Professor Phillip Sprangle, Chair
Professor Thomas Antonsen
Professor Howard Milchberg
Professor Rajarshi Roy (Dean's Representative)
Dr. Joseph Peñano
Dr. Antonio Ting

Acknowledgements

There are many people without whom this dissertation would not have been possible.

First, I must thank my doctoral advisor and mentor, Prof. Phillip Sprangle. I could not have asked for a more knowledgeable and experienced guide in my graduate career. He has been generous with both his time and his advice, meeting me where I am in my education but also expecting of me things I did not know I could accomplish. He was patient of my initial ignorance and occasional stumble, but never stopped pushing me to grow as a scientist, and for that I will always be grateful.

I'd like to thank Professor Tom Antonsen, Professor Howard Milchberg, Professor Rajarshi Roy, Dr. Joe Penano and Dr. Tony Ting, for agreeing to serve on my advisory committee and for their generous contribution of the time required to do so. I'd particularly like to thank Prof. Milchberg, Dr. Penano, and Dr. Ting for numerous valuable discussions.

Additionally, I'm grateful to Dr. Luke Johnson and Dr. Bahman Hafizi at the Naval Research Laboratory, as well as Daniel Woodbury and Robert Schwartz in Prof. Milchberg's group, for fruitful discussions and communication.

I have had the pleasure of sharing an office with Zachary Epstein, Thomas Rensink, Chenlong Miao, Evan Dowling, and Paul Gradney, and I'm grateful to each one for the part they have played in making 3326 A.V. Williams a warm and welcoming environment. I have a great deal of fondness for this place, and I have all of you to thank for that.

Thank you to my girlfriend Meshan, who has supported and encouraged me more than I could possibly have asked, and without whose presence my life and work would be diminished.

Thank you to my parents, for the curiosity and love of knowledge they have instilled in me, and for the support they've given me at every step of my education.

Table of Contents

3   Proton acceleration in a slow wakefield

List of Tables

List of Figures

Introduction

This dissertation is composed of three chapters, each of which has been separately published in a peer-reviewed journal. They deal broadly with the topic of intense laser matter interactions, from the perspective of basic physics, but with real-world applicability firmly in mind. The chapters are, in the order in which they appear in this dissertation:

1. The effect of laser noise on the propagation of laser radiation in dispersive and nonlinear media (published in the Journal of the Optical Society, B, in 2019 [1]),

2. Remote detection of radioactive material using optically induced air breakdown ionization (published in Physics of Plasmas in 2016 [2], with experimental proof-of-concept published in Science Advances in 2019 [3]), and

3. Proton acceleration in a slow wakefield (published in Applied Physics letters in 2017 [4]).

In the first chapter, the effect of laser noise on the atmospheric propagation of high-power CW lasers and high-intensity short pulse lasers in dispersive and nonlinear media is studied. We consider the coupling of laser intensity noise and phase noise to the spatial and temporal evolution of laser radiation. High-power CW laser systems have relatively large fractional levels of intensity noise and frequency noise. We show that

laser noise can have important effects on the propagation of high-power as well as high-intensity lasers in a dispersive and nonlinear medium such as air. A paraxial wave equation, containing dispersion and nonlinear effects, is expanded in terms of fluctuations in the intensity and phase. Longitudinal and transverse intensity noise and frequency noise are considered. The laser propagation model includes group velocity dispersion, Kerr, delayed Raman response, and optical self-steepening effects. A set of coupled linearized equations are derived for the evolution of the laser intensity and frequency fluctuations. In certain limits these equations can be solved analytically. We find, for example, that in a dispersive medium, frequency noise can couple to, and induce, intensity noise (fluctuations), and vice versa. At high intensities the Kerr effect can suppress this intensity noise. In addition, significant spectral modification can occur if the initial intensity noise level is sufficiently high. Finally, our model is used to study the transverse and longitudinal modulational instabilities. We present atmospheric propagation examples of the spatial and temporal evolution of intensity and frequency fluctuations due to noise for laser wavelengths of $0.85\ \mu m$, $1\ \mu m$, and $10.6\ \mu m$.

In the second chapter, a concept for all-optical remote detection of radioactive materials is presented and analyzed. The presence of excess radioactivity increases the level of negative ions in the surrounding air region. This can act as a source of seed electrons for a laser-induced avalanche ionization breakdown process. We model irradiated air to estimate the density of negative ions and use a set of coupled rate equations to simulate a subsequent laser-induced avalanche ionization. We examine avalanche ionization behavior in several laser parameter regimes, and determine the time

required for saturation of the breakdown for both a single seed ion, as well as for a population of ions present in the focused volume of a high-intensity laser pulse. These correspond to two methods of remotely measuring the ion density, which is a signature of radioactive materials.

Finally, in the third chapter, we propose and analyze a mechanism to accelerate protons in a low-phase-velocity wakefield, a type of plasma wave. The wakefield is shock-excited by the interaction of two counter-propagating laser pulses in a plasma density gradient. The laser pulses consist of a forward-propagating short pulse (less than a plasma period) and a counter-propagating long pulse. The beating of these pulses generates a slow forward-propagating wakefield that can trap and accelerate protons. The trapping and acceleration is accomplished by appropriately tapering both the plasma density and the amplitude of the backward-propagating pulse. An example is presented in which the trapping and accelerating wakefield has a phase velocity varying from $V_{ph} \approx 0$ to $\approx 0.15\,c$ $(\sim 10\,\text{MeV}$ proton energy) over a distance of ~ 1 cm. The required laser intensities, pulse durations, pulse energies and plasma densities are relatively modest. Instabilities such as the Raman instability are mitigated due to the large plasma density gradients. Numerical solutions of the wakefield equation and simulations using turboWAVE are carried out to support our model.

Chapter 1. The effect of laser noise on the propagation of laser radiation in dispersive and nonlinear media

1.1. Introduction

High average power CW (greater than 10 kW) and high-intensity (up to 1 TW/cm^2) short pulse lasers (with pulse lengths ranging from hundreds of femtoseconds to greater than a nanosecond) play important roles in a number of areas such as active and passive remote sensing [2], [5–9], power beaming [10], communications, directed energy [10], [11], electronic counter measures and induced electric discharges (artificial lighting) [12], [13]. In addition, high-intensity short pulse lasers are employed for fundamental high-intensity laser matter interaction and nonlinear optics studies. These applications include Raman amplification [14], laser driven particle acceleration [4], ultra-high frequency radiation generation and beacon beam (guide stars) generation [15], [16].

Common to many of these applications is the requirement to propagate the laser radiation over distances of many Rayleigh lengths, either through the atmosphere or in a nonlinear medium. In general, laser noise can play an important role on the propagation characteristics of the radiation. The laser noise considered here consists of phase noise, as well as temporal and spatial intensity noise. For example, high average power CW lasers,

which have directed energy applications, have large line-widths due to frequency noise. When these laser pulses propagate in the atmosphere, the relatively large frequency spreads induce intensity fluctuations due to atmospheric dispersion. Additionally, atmospheric nonlinearities and dispersion play important roles in the long range propagation of high-intensity, short laser pulses. The nonlinearities in the atmosphere can couple the various components of laser noise and lead to disruptive instabilities.

In this analysis, we carry out computational examples for two classes of laser systems. These are the high-intensity, short pulse lasers having wavelengths $\lambda_0 = 0.85$ μm and $\lambda_0 = 10.6$ μm, for which nonlinear and dispersion effects are important, and high-average power lasers having wavelengths $\lambda_0 = 1$ μm for which nonlinear effects may be neglected but dispersion can play an important role.

1.2. Formulation of Laser Noise

In this analysis, a paraxial wave equation, containing dispersion and nonlinear effects, is expanded in terms of fluctuations in the intensity and phase due to noise. We model the laser field as a CW beam with longitudinal and transverse intensity noise and frequency noise. Our laser propagation model includes Kerr nonlinearities, group velocity dispersion, delayed Raman response, and optical self-steeping. Ionization effects are not included.

The laser electric field satisfies the wave equation [17], [18],

$$\nabla^2 E(\mathbf{r},t) - \frac{1}{c^2}\frac{\partial^2 E(\mathbf{r},t)}{\partial t^2} = \frac{4\pi}{c^2}\left(\frac{\partial^2 P_L(\mathbf{r},t)}{\partial t^2} + \frac{\partial^2 P_{NL}(\mathbf{r},t)}{\partial t^2}\right) \qquad (1.1)$$

$$E(\mathbf{r},t) = \frac{1}{2}\hat{\mathbf{e}}_{\perp}\hat{E}(\mathbf{r},t)e^{ik_0 z - i\omega_0 t} + c.c.$$
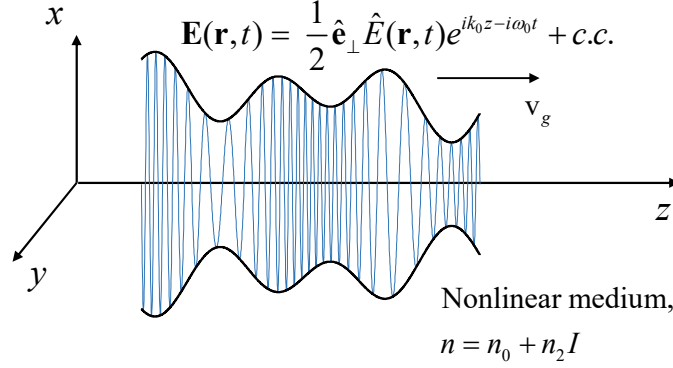
Figure 1.1. Diagram of a pulse with intensity and frequency noise, propagating in a medium with a nonlinear contribution to the total index of refraction.

where $E(\mathbf{r},t) = \mathrm{Re}[\hat{E}(\mathbf{r},t)\exp(i(k_0 z - \omega_0 t))]$, $\hat{E}(\mathbf{r},t)$ is the complex amplitude, ω_0 is the carrier frequency, $k_0 = n_0(\omega_0)\omega_0/c$ is the carrier wavenumber, $n_0(\omega)$ is the frequency dependent linear refractive index, and $P_L(\mathbf{r},t) = \mathrm{Re}[\hat{P}_L(\mathbf{r},t)\exp(i(k_0 z - \omega_0 t))]$ and

$P_{NL}(\mathbf{r},t) = \mathrm{Re}[\hat{P}_{NL}(\mathbf{r},t)\exp(i(k_0 z - \omega_0 t))]$ are, respectively, the linear and nonlinear polarization fields. Free charges and currents are neglected, and the electric field is taken to be linearly polarized. Figure 1.1 shows a pulse in this coordinate system, with intensity and phase noise, propagating in a nonlinear medium.

Substituting this field representation into the wave equation and transforming to the group velocity frame leads to a paraxial wave equation for the complex laser amplitude. The paraxial wave equation for $\hat{E}(\mathbf{r},t)$ is

$$\nabla_\perp^2 \hat{E} + \frac{\partial^2 \hat{E}}{\partial z^2} + 2ik_0 \left(1 + \frac{i}{v_g k_0} \frac{\partial}{\partial \tau}\right) \frac{\partial \hat{E}}{\partial z}$$

$$- k_0 \left(\beta_2 - i\frac{\beta_3}{3}\frac{\partial}{\partial \tau} + \ldots\right)\frac{\partial^2 \hat{E}}{\partial \tau^2} + 4\pi \frac{\omega_0^2}{c^2}\left(1 + \frac{i}{\omega_0}\frac{\partial}{\partial \tau}\right)^2 \hat{P}_{NL} = 0, \qquad (1.2)$$

where $\nabla_\perp^2 = \partial^2/\partial x^2 + \partial^2/\partial y^2$, β_2 is the group-velocity dispersion (GVD) coefficient,

β_3 is the third order dispersion coefficient and the group velocity is

$v_g = c(\partial(\omega n_0)/\partial \omega)^{-1} \approx \omega_0/k_0$. The GVD parameter can be defined as

$\beta_2 = \partial(1/v_g)/\partial \omega \big|_{\omega=\omega_0}$. In obtaining Eq. 1.2 it was convenient to transform the wave

equation to the group velocity frame, $\tau = t - z/v_g$ and $\eta = z$. The propagation distance

variable η has been replaced with the more conventional notation z and the amplitude $\hat{E}$

was assumed to vary slowly in space and time compared with the rapidly varying carrier

term, $\exp(i(k_0 z - \omega_0 t))$. Neglecting higher order derivatives in z and τ, i.e.,

$\partial^2/\partial z^2$, $\partial^3/\partial \tau^3$, $\nabla_\perp^2 \partial/\partial \tau$ and higher, and setting the group velocity equal to the phase

velocity $v_g = \omega_0/k_0$, Eq. 1.2 reduces to

$$\nabla_\perp^2 \hat{E} + 2ik_0 \frac{\partial \hat{E}}{\partial z} - k_0 \beta_2 \frac{\partial^2 \hat{E}}{\partial \tau^2} + 4\pi \frac{\omega_0^2}{c^2}\left(1 + \frac{i}{\omega_0}\frac{\partial}{\partial \tau}\right)\hat{P}_{NL} = 0. \qquad (1.3)$$

The nonlinear polarization field for the Kerr effect is proportional to the

convolution of the intensity with a response function [17], [19],

$\hat{P}_{NL} = \frac{\gamma_{NL} n_0 c}{2\pi \omega_0} \hat{E}(z,\tau) \int_{-\infty}^{\tau} R(\tau')I(z,\tau-\tau')d\tau'$, where $\gamma_{NL} = \omega_0 n_2/c$ characterizes the Kerr

nonlinearity, n_2 is the nonlinear Kerr refractive index, $I = \kappa_0 |\hat{E}|^2$ is the intensity, and

$\kappa_0 = n_0 c \epsilon_0 / 2$. For an instantaneous nonlinear response, $R(\tau) = \delta(\tau)$, equivalent to the

susceptibility $\chi^{(3)}$ being constant with respect to the frequency. In general, the nonlinear

polarization is composed of an instantaneous electronic response and a delayed Raman

response, $R(\tau) = \delta(\tau)(1 - f_R) + f_R h_R(\tau)$, where f_R is the fraction of the nonlinear

response due to Raman effects and $h_R(\tau)$ is the Raman response function.

In the limit of the linearized Raman response, the Fourier transform of the Raman

response function is approximated as $\tilde{h}_R(\omega) \approx 1 + i\omega B$, where B is a slope parameter [19].

In this limit, the nonlinear polarization field amplitude is

$\hat{P}_{NL} = \left(\gamma_{NL} n_0 c / (2\pi \omega_0) \right)\left(I - \tau_R \partial I / \partial \tau \right) \hat{E}$, [17], [18], and Eq. 1.3 becomes

$$\nabla_{\perp}^2 \hat{E} + 2ik_0 \frac{\partial \hat{E}}{\partial z} - k_0 \beta_2 \frac{\partial^2 \hat{E}}{\partial \tau^2} + 2k_0 \gamma_{NL} \left(I\hat{E} + \frac{i}{\omega_0} \frac{\partial(I\hat{E})}{\partial \tau} - \tau_R \frac{\partial I}{\partial \tau} \hat{E} \right) = 0. \quad (1.4)$$

The term proportional to $\partial(I\hat{E})/\partial\tau$ is responsible for optical shock formation, and

$\tau_R = f_R B$ is a time characterizing the delayed Raman response [17], [18]. For 800 nm

pulse in air, this time is $\sim$ 100 fs [20]. In the absence of the Raman response and optical

shock terms, the total refractive index is given by $n = n_0 + n_2 I$.

We now represent the complex field amplitude as $\hat{E} = A \exp(i\varphi)$, where the

amplitude A and phase φ are real and functions of x, y, z, τ. Substituting the complex

amplitude representation into Eq. 4 and equating real and imaginary parts yield a set of coupled equations for A and φ,

$$
\frac{\partial A}{\partial z} - \frac{\beta_2}{2}\left(2\frac{\partial \varphi}{\partial \tau}\frac{\partial A}{\partial \tau} + \frac{\partial^2 \varphi}{\partial \tau^2}A \right) + 3\gamma_{NL}\kappa_0 A^2 \frac{1}{\omega_0}\frac{\partial A}{\partial \tau}
$$
$$
+ \frac{A}{2k_0}\nabla_\perp^2 \varphi + \frac{1}{k_0}(\nabla_\perp \varphi)\cdot(\nabla_\perp A) = 0,
$$
(1.5a)

$$
\frac{\partial \varphi}{\partial z}A + \frac{\beta_2}{2}\left(\frac{\partial^2 A}{\partial \tau^2} - \left(\frac{\partial \varphi}{\partial \tau}\right)^2 A \right) - \gamma_{NL}\kappa_0 A^3\left(1 - \frac{1}{\omega_0}\frac{\partial \varphi}{\partial \tau} - 2\frac{\tau_R}{A}\frac{\partial A}{\partial \tau} \right)
$$
$$
- \frac{1}{2k_0}\nabla_\perp^2 A + \frac{1}{2k_0}(\nabla_\perp \varphi)\cdot(\nabla_\perp \varphi)A = 0.
$$
(1.5b)

1.2.1. Linearization of propagation equation

The amplitude and frequency spread are expanded (linearized) about a plane wave solution of the coupled equations in Eq. 1.5a,b. The amplitude and phase are expressed as a zeroth-order and a perturbed part, i.e., $A = A_0 + \delta A(x,y,z,\tau)$, $\varphi = \varphi_0(z) + \delta\varphi(x,y,z,\tau)$, where the amplitude and normalized frequency perturbations, i.e., δA and $\delta\omega = -\omega_0^{-1}\partial\delta\varphi/\partial\tau$, are assumed to be small, i.e., $|\delta A| \ll A_0$ and $|\delta\omega| \ll 1$. Note that the phase $\delta\varphi$ is not considered a small quantity. However, the perturbed frequency spread is indeed small compared with the carrier frequency ω_0. The normalized perturbed wavenumber is $\delta k = k_0^{-1}(\partial/\partial z - v_g^{-1}\partial/\partial\tau)\delta\varphi$ and is small compared to unity, i.e., $|\delta k| \ll 1$. The perturbed frequency and wavenumber are normalized to ω_0 and k_0,

respectively. Under these conditions the perturbed amplitude and phase are given by the following coupled equations,

$$\frac{\partial \delta A}{\partial z} = \frac{\beta_2}{2} \frac{\partial^2 \delta \varphi}{\partial \tau^2} A_0 - 3 k_{NL} \frac{1}{\omega_0} \frac{\partial \delta A}{\partial \tau} - \frac{A_0}{2 k_0} \nabla_\perp^2 \delta \varphi , \qquad (1.6a)$$

$$A_0 \frac{\partial \delta \varphi}{\partial z} = -\frac{\beta_2}{2} \frac{\partial^2 \delta A}{\partial \tau^2} + 2 k_{NL} \, \delta A - \gamma_{NL} I_0 \frac{A_0}{\omega_0} \frac{\partial \delta \varphi}{\partial \tau}$$
$$- 2 k_{NL} \, \tau_R \frac{\partial \delta A}{\partial \tau} + \frac{1}{2 k_0} \nabla_\perp^2 \delta A , \qquad (1.6b)$$

where $k_{NL} = \gamma_{NL} I_0$, $I_0 = \kappa_0 A_0^2$ is the equilibrium intensity and the zeroth-order phase is found from Eq. 1.5b to be $\varphi_0 = \gamma_{NL} I_0 z$. It is convenient to rewrite Eqs. 1.6 in terms of the normalized perturbed intensity $\delta I(\mathbf{r}, \tau) = I(\mathbf{r}, \tau) / I_0 - 1 = 2 \delta A / A_0$,

$$\frac{\partial \delta I}{\partial z} = \beta_2 \frac{\partial^2 \delta \varphi}{\partial \tau^2} - 3 k_{NL} \frac{1}{\omega_0} \frac{\partial \delta I}{\partial \tau} - \frac{1}{k_0} \nabla_\perp^2 \delta \varphi , \qquad (1.7a)$$

$$\frac{\partial \delta \varphi}{\partial z} = -\frac{\beta_2}{4} \frac{\partial^2 \delta I}{\partial \tau^2} - k_{NL} \frac{1}{\omega_0} \frac{\partial \delta \varphi}{\partial \tau} + k_{NL} \left(\delta I - \tau_R \frac{\partial \delta I}{\partial \tau} \right) + \frac{1}{4 k_0} \nabla_\perp^2 \delta I . \qquad (1.7b)$$

We now transform into frequency space, with the tilde denoting the Fourier transform in τ, x, and y,

$$\tilde{Q}(z, \omega, k_x, k_y) = \int_{-\infty}^{+\infty} Q(z, \tau, x, y) \exp(-i(\omega \tau + k_x x + k_y y)) \, d\tau \, dx \, dy .$$

Taking the Fourier transforms of Eqs. 1.7a,b in τ, x and y, the normalized intensity and frequency perturbations are given by,

$$\frac{\partial \delta \tilde{I}}{\partial z} = -i K_0 \frac{\omega_0}{\omega} \delta \tilde{\omega} - 3 i k_{NL} \frac{\omega}{\omega_0} \delta \tilde{I}, \qquad (1.8a)$$

$$\frac{\partial \delta \tilde{\omega}}{\partial z} = -\frac{i}{4} \frac{\omega}{\omega_0} \left(K_0 + 4 k_{NL} (1 - i \tau_R \omega) \right) \delta \tilde{I} - i k_{NL} \frac{\omega}{\omega_0} \delta \tilde{\omega}, \qquad (1.8b)$$

where $\delta \tilde{\omega} = -i (\omega / \omega_0) \delta \tilde{\varphi}$, $K_0 = \beta_2 \omega^2 - k_\perp^2 / k_0$, $k_\perp^2 = k_x^2 + k_y^2$ and $|\omega| \ll \omega_0$.

Combining Eqs. 1.8a,b gives

$$\frac{\partial^2}{\partial z^2} \begin{pmatrix} \delta \tilde{I} \\ \delta \tilde{\omega} \end{pmatrix} + 4 i k_{NL} \frac{\omega}{\omega_0} \frac{\partial}{\partial z} \begin{pmatrix} \delta \tilde{I} \\ \delta \tilde{\omega} \end{pmatrix} + $$
$$\left(\frac{K_0^2}{4} + K_0 k_{NL} (1 + i \tau_R \omega) - 3 k_{NL}^2 \frac{\omega^2}{\omega_0^2} \right) \begin{pmatrix} \delta \tilde{I} \\ \delta \tilde{\omega} \end{pmatrix} = 0. \qquad (1.9)$$

Equation 1.9 can be solved for the Fourier transforms $\delta \tilde{I}$ and $\delta \tilde{\omega}$ as a function of the propagation distance z.

Before proceeding with a full numerical treatment of Eq. 1.9 it is useful to consider some limiting cases analytically. Neglecting the small terms of order $k_{NL} \omega / \omega_0$ and Raman effects, i.e., $\tau_R = 0$, Eq. 1.9 reduces to $(\partial^2 / \partial z^2 + K^2)(\delta \tilde{I}, \delta \tilde{\omega}) = 0$, with solutions

$$\delta \tilde{I}(z, \omega, k_\perp) = \delta \tilde{I}(0, \omega, k_\perp) \cos(K z) - i \frac{\omega_0}{\omega} \frac{K_0}{K} \delta \tilde{\omega}(0, \omega, k_\perp) \sin(K z), \qquad (1.10a)$$

$$\delta\tilde{\omega}(z,\omega,k_\perp)=\delta\tilde{\omega}(0,\omega,k_\perp)\cos(Kz)-i\frac{\omega}{\omega_0}\frac{K}{K_0}\delta\tilde{I}(0,\omega,k_\perp)\sin(Kz), \qquad (1.10b)$$

where $K^2 = K_0^2/4 + K_0\,k_{NL}$ and initial conditions have been applied using Eqs. 1.8a,b.

Equations 1.10a,b clearly show the coupling between intensity and frequency noise.

1.2.2. Dispersion relation

It is useful to consider the various regions of instability by examining the dispersion relation for the perturbation system described by Eqs. 1.10a,b. To obtain the dispersion relation, we take $\delta\tilde{I}$ and $\delta\tilde{\varphi}$ to vary like $\exp(i\,k\,z)$, and Eq. 1.9 then yields the dispersion relation,

$$k^2 + 4k_{NL}\,k\,\omega/\omega_0 - K_0(K_0/4 + k_{NL}(1-i\,\tau_R\,\omega)) + 3k_{NL}^2\,\omega^2/\omega_0^2 = 0. \qquad (1.11)$$

A more accurate dispersion relation may be found in Appendix 1.A, which includes terms that go like $\partial^2/\partial z^2$, $\partial^2/\partial z\partial\tau$, etc. For parameters relevant to this analysis, however, most additional terms in the dispersion relation are small.

The dispersion relation in Eq. 1.11 has a number of regions of instability. For example, in the case where $k_{NL}|\omega|/\omega_0 \ll k$ and $\tau_R = 0$, the dispersion relation reduces to

$$k = \pm(1/2k_0)\sqrt{(k_\perp^2 - \beta_2\,\omega^2\,k_0)(k_\perp^2 - \beta_2\,\omega^2\,k_0 - 4k_0k_{NL})} = \pm\,K. \qquad (1.12)$$
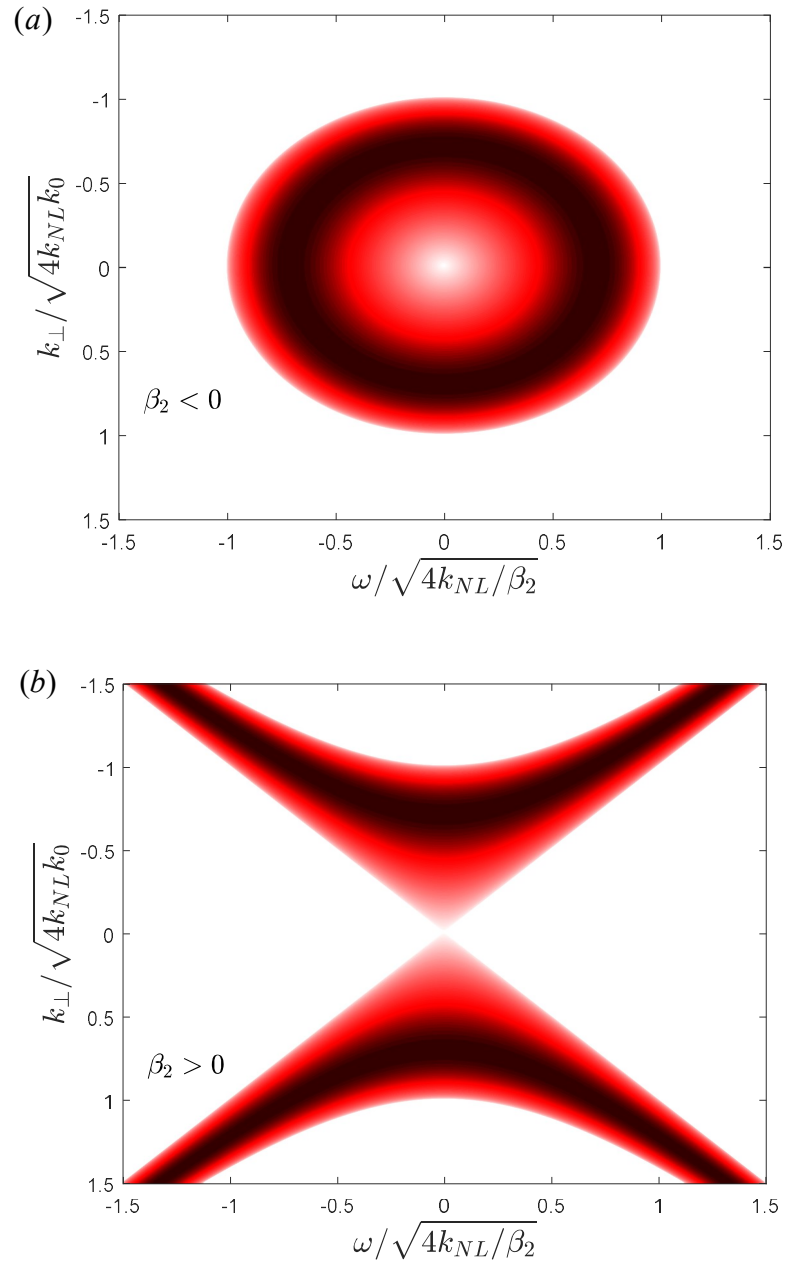
Figure 1.2. Growth rate of modulational instability, $\Gamma = \text{Im}[k]$, as a function of $k_\perp$ and ω (Eq. 1.12), for (a) anomalous and (b) normal group-velocity dispersion. The maximum growth rate is $\Gamma_{max} = k_{NL} = (\omega_0 / c) n_2 I_0$.

Both the intensity and frequency perturbations are unstable when $\text{Im}[k] < 0$, which

requires that the nonlinear term k_{NL} be nonzero. For positive k_{NL} ($n_2 > 0$), the optical

beam is unstable when $0 < k_\perp^2 - \beta_2\,\omega^2\,k_0 < 4k_0\,k_{NL}$. The maximum growth rate occurs

for $k_\perp^2 = 2k_0\,k_{NL} + \beta_2\,\omega^2\,k_0$ and has the value $\Gamma_{max} = \text{Im}[k]_{max} = k_{NL} = (\omega_0/c)n_2 I_0$.

Figure 1.2 shows the growth rate as a function of $k_\perp$ and ω for positive and negative β_2.

The white areas indicate regions of stability, while the colored regions have $\text{Im}[k] \neq 0$,

with black indicating the maximum. The axes are normalized to values of $k_\perp$ and ω

($\beta_2 < 0$) for which $k = 0$.

In the absence of transverse variations, $k_\perp = 0$, the optical beam is unstable when

the group velocity coefficient β_2 is negative and the frequency of the instability satisfies

the condition $0 < |\beta_2|\omega^2 < 4k_{NL}$. In the case where $\beta_2 = 0$ and $k_\perp^2 \neq 0$ instability

occurs for $0 < k_\perp^2 < 4k_{NL}\,k_0$. These are, respectively, the longitudinal and transverse

modulation instabilities [17], [21].

The Kerr nonlinear focusing power $P_{Kerr} = \lambda_0^2/(2\pi n_0\,n_2)$, [11], [18], [22], can be

estimated from knowledge of the transverse modulational instability's growth rate. For a

laser beam having a spot size R_s and for $\beta_2 = 0$, the maximum growth rate occurs for

$1/R_s^2 \approx 2n_2(\omega_0/c)I_0\,k_0 = 2n_0\,n_2(\omega_0/c)^2 I_0$, where we have set $k_\perp = \sqrt{2k_{NL}\,k_0} \sim 2/R_s$.

For a Gaussian beam profile the radiation power is $P = I_0(\pi R_s^2/2)$. Setting

$R_s^2 \approx 1/(2n_0\,n_2(\omega_0/c)^2 I_0)$ we find that the maximum growth rate occurs for a beam

power of $P \approx \lambda_0^2 / (4\pi n_0 n_2)$. Apart from a numerical factor this is just the nonlinear

focusing power P_{Kerr} which is responsible for laser filamentation.

A similar analysis may be performed in the longitudinal 1-D case ($k_\perp = 0$). For a

pulse of duration τ_L, instabilities cannot be seeded at frequencies below $\omega_{min} \sim (2/\tau_L)$.

In this case, the longitudinal instability, which occurs for $|\beta_2| \omega^2 < 4k_{NL}$, requires an

intensity $I_0 > \gamma_{NL} |\beta_2| / \tau_L^2$ in order for growth to occur.

An analysis of pulses which are finite in both spot size and duration can be found

in Appendix 1.B. We find that for $\beta_2 < 0$, there are parameters which can lead to pulses

which do not change in duration or spot size when they propagate in a nonlinear medium.

1.2.3. Saturation of the longitudinal instability

For the transverse modulational instability, under most circumstances, the

instability grows until the peak intensity is sufficient for ionization to arrest the process.

For the longitudinal modulational instability, however, ionization is not necessary –

saturation of the instability occurs for the nonlinear Schrodinger equation (Eq. 1.4)

without the inclusion of additional effects.

The maximum growth rate for the longitudinal modulational instability occurs for

$\omega_{max} = \sqrt{2k_{NL} / |\beta_2|}$. The instability will then grow with the period

$\tau_{max} = 2\pi / \omega_{max} = 2\pi \sqrt{|\beta_2| c / (2\omega_0 n_2 I_0)}$. As the instability progresses into the non-

perturbative regime, it forms a periodic train of micro-pulses [23], each separated by the

duration τ_{max}, with width $\Delta T(z)$ and a constant total energy per unit area $J_0 = \tau_{max} I_0$.

These micro-pulses have a broad spectrum, with much of the power spectrum lying outside the spectral region of the growth rate. This will substantially reduce the growth of the instability.

The dynamics of the width $\Delta T(z)$ of each micro-pulse may be approximated (Appendix 1.B) as

$$\frac{\partial^2 \Delta T}{\partial z^2} = \frac{4\beta_2^2}{\Delta T^3}\left(1 - \frac{\pi J_0}{2P_{Kerr} k_0 |\beta_2|}\Delta T\right) \tag{1.13}$$

where the substitution $E_0 / R^2 = \pi J_0 / 2$ has been used and the spot size has been assumed to be constant. If there is no initial chirp, the micro-pulse duration has a steady-state solution $\Delta T_{sat} = 2P_{Kerr} k_0 |\beta_2| / \pi \tau_{max} I_0$, with $\Delta T_{sat} / \tau_{max} = 2/\pi^2 \approx 1/5$. The ratio of the FWHM of the micro-pulse power spectrum at saturation to the frequency of maximum growth rate is therefore $\Delta\omega_{sat} / \omega_{max} \gtrsim 2$, hence much of the power is outside of the growth rate spectrum.

A stability analysis using $\Delta T = \Delta T_{sat} + \epsilon$ gives the equation $\partial^2 \epsilon / \partial z^2 = -(4\beta_2^2 / \Delta T_{sat}^4)\epsilon$, so Eq. 1.13 is stable for perturbations around ΔT_{sat}. In other words, the duration of the individual micro-pulses reaches a stable value, saturating the instability.

Simulations of this instability and its saturation are shown in the next section.

1.3. Simulation of laser propagation in air

In this section, we present some computational examples of noise in laser systems and its effect on atmospheric propagation. The computational examples of Eqs. 1.10a,b are carried out for two classes of laser systems. These are the high-intensity, short pulse lasers having a wavelength $\lambda_0 = 0.85\ \mu m$ and $.\lambda_0 = 10.6\ \mu m$., for which nonlinear and dispersion effects are important, and for high-average power lasers having wavelength $\lambda_0 = 1\ \mu m$, for which nonlinear effects are less important but dispersion can play an important role. We demonstrate coupling of frequency and intensity noise at several values of the average intensity. For sufficient levels of initial intensity noise when the peak intensity is very high, we show significant spectral broadening. Finally, we use our model to demonstrate the effect of various types of noise on the transverse and longitudinal modulational instabilities for a high-intensity pulse.

Some of the typical parameters used in the computations in this section are shown in Table 1.1. The parameters in Table 1.1 correspond to the values associated with laser propagation in the atmosphere.

1.3.1. Initial laser noise

In our examples, we model the frequency noise input at $z = 0$ as band-limited white noise, expressed as

$$\delta\omega(0,\tau) = \sum_{n=0}^{N_\tau/2} R_{n,\omega}\,\Theta\!\left(\omega_B - \omega_n\right)\cos\!\left(\omega_n \tau + \theta_{n,\omega}\right), \tag{1.14}$$

	$n_2 [10^{-19} \text{cm}^2/\text{W}](a)$	$\beta_2 [\text{fs}^2/\text{cm}]$	$P_{Kerr} [\text{GW}](b)$
0.85	4, [18]	0.21, [22]	3
1	4, [18]	0.17, [22]	4
10.6	4, [23]	-0.3, [24], [25] (c)	450

Table 1.1: The laser wavelengths and parameters used in the examples. (a) The long-pulse limit (> 150 fs) is used for the nonlinear index n_2, which includes rotational effects. (b) The expression for the nonlinear focusing power used in our analysis is $P_{Kerr} = \lambda_o^2 / (2\pi n_0 n_2)$. (c) The GVD parameter β_2 for $\lambda_0 = 10.6$ μm has been calculated for 50% relative humidity.

where $\omega_n = 2\pi n / T$, $R_{n,\omega}$ are a set of normal random numbers with zero mean, and $\theta_{n.\omega}$ are uniform random numbers on the interval $[0, 2\pi]$. The full frequency noise bandwidth is $2\omega_B$, and Θ denotes the Heaviside step function. The total measurement time is $T = N_\tau \Delta t$, where N_τ is the number of temporal grid points and Δt is the temporal grid spacing. The instantaneous frequency is normalized so that its standard deviation is $\sigma(\delta\omega) = (\omega_B \Omega_\omega / \pi)^{1/2} / \omega_0$, where Ω_ω is the frequency noise level, and is also the linewidth if $\Omega_\omega \ll \omega_B$. The phase fluctuation can be calculated using the definition of the normalized frequency fluctuation, $\delta\omega = -\omega_0^{-1} \partial \delta\varphi / \partial\tau$, and, depending on the value of ω_B, can be a 1-D Brownian walk. An example of the numerically generated frequency and phase fluctuations is shown in Fig. 1.3.

The normalized input intensity noise at $z = 0$ is represented as Lorentzian noise,
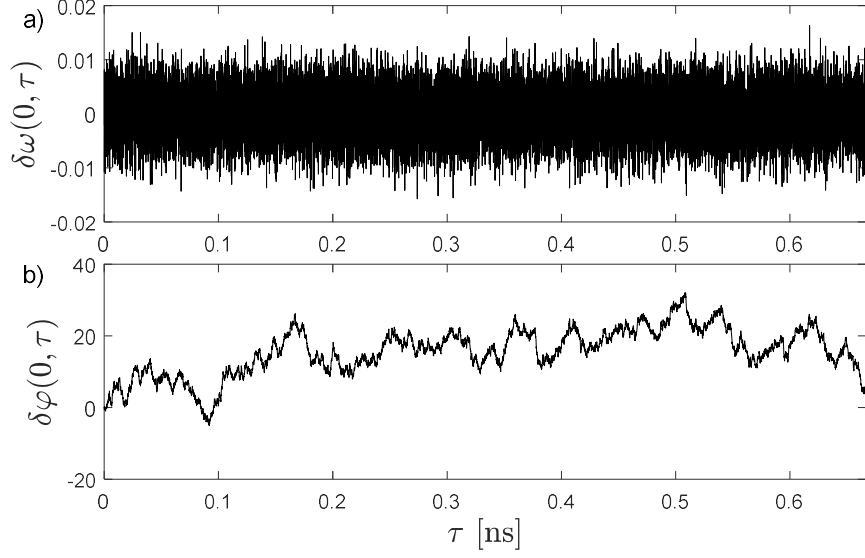
Figure 1.3. Shows a) frequency and b) corresponding phase fluctuations as described in Eq. 1.14. Parameters are $\lambda_0 = 1 \ \mu m$, $\Delta\omega / \omega_0 = \Omega_\omega / \omega_0 = 10^{-3}$, $2\omega_B / \omega_0 = 10^{-1}$, $\omega_0 \Delta t = 19.2$, and $N_\tau = 2^{16}$. For these parameters, the condition $\delta\omega \ll 1$ is satisfied.

$$\delta I(0, \tau) = \sum_{n=0}^{N_\tau/2} R_{n,I} \, L(\omega_n) \cos\left(\omega_n \tau + \theta_{n,I}\right), \tag{1.15}$$

where the parameters are analogous to the parameters in the frequency noise expression, Eq. 1.14, and $L(\omega) = 1 / \sqrt{\Omega_I^2 + \omega^2}$ denotes the intensity spectral function and Ω_I is the intensity spectral width.

These representations for the frequency and intensity fluctuations are equivalent to directly specifying the discrete Fourier transform of these quantities. The analytical solutions to the propagation system, Eqs. 1.10a,b, can also be expressed in this

formulation. For example, in 1-D, if there is only initial intensity noise, Eq. 1.15, and the frequency noise at $z = 0$ is $\delta\omega(0, \tau) = 0$, the final intensity noise is

$$\delta I(z, \tau) = \sum_{n=0}^{N_\tau/2} R_{n,I} \, L(\omega_n) \cos\left(\omega_n \tau + \theta_{n,I}\right) \cos\left(K_n\right), \qquad (1.16a)$$

and the final frequency noise is

$$\delta\omega(z, \tau) = \sum_{n=0}^{N_\tau/2} \frac{K_n \, \omega_n}{\beta_2 \, \omega_0} R_{n,I} \, L(\omega_n) \cos\left(\omega_n \tau + \theta_{n,I}\right) \sin\left(K_n\right), \qquad (1.16b)$$

where $K_n = \sqrt{(\beta_2 \, \omega_n^2)^2 / 4 + \beta_2 \, \omega_n^2 \, k_{NL}}$. This shows that in a dispersive medium such as air, initial intensity noise leads to frequency noise. The reverse process also occurs, as we will demonstrate in a later section.

The power spectrum for a random function $F(t)$ with Fourier transform $\tilde{F}(\omega)$ is defined as $P(\omega) \equiv (1/T)\langle|\tilde{F}(\omega)|^2\rangle$, where T is the measurement time period and $\langle\,\rangle$ denotes an average over many realizations of $F(t)$. The normalized frequency, Eq. 1.14, has spectrum $P_{\delta\omega}(0, \omega) = \Omega_\omega / \omega_0^2$, and the spectrum of the intensity is

$$P_{\delta I}(0, \omega) \propto L^2(\omega) = 1/\left(\Omega_I^2 + \omega^2\right).$$

The instantaneous frequency, i.e. $-\partial\delta\varphi/\partial\tau$, is important in that its spectrum can help characterize a particular laser system. The distribution of instantaneous frequencies does not, however, represent the photonic frequency content of a laser beam. A more physically relevant measure of the beam's spectral content is the power spectrum
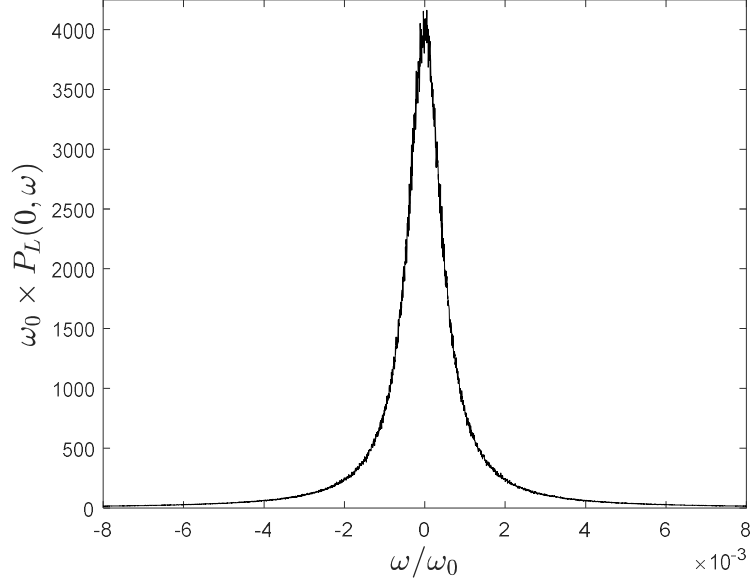
Figure 1.4. Average normalized laser field power spectrum $P_L(0, \omega)$ for an ensemble of $N_{ens} = 1000$ samples. Each sample was generated with frequency fluctuations described in Eq. 1.14, and no intensity fluctuations. Parameters are those used in Fig. 1.2.

$P_L(z, \omega)$ of the normalized total field envelope, i.e. $(A(z, \tau)/A_0) \exp(i\, \delta\varphi(z, \tau))$, where the equilibrium phase $\varphi_0(z)$ is time-independent. For the frequency noise described in Eq. 1.14 and a fixed noise level Ω_ω, the spectral lineshape may be Gaussian, Lorentzian, or some intermediary function, depending on the frequency noise cutoff ω_B, [24]. For $\omega_B \gg \Omega_\omega$, the laser line is Lorentzian with a linewidth $\Delta\omega = \Omega_\omega$. For $\omega_B \ll \Omega_\omega$, the line is a Gaussian with linewidth $\Delta\omega = \left(2\ln(2)\Omega_\omega \omega_B / \pi^2\right)^{1/2}$. In either case, the phase undergoes a random wander of order 2π on a time scale equal to the coherence time

$\tau_c = 2\pi / \Delta\omega$. Figure 1.4 shows the average spectral line for parameters given in Fig. 1.3, which yield a Lorentzian shape. The ensemble is composed of $N_{ens} = 1000$ samples.

1.3.2. Transfer of frequency noise to intensity noise in a dispersive medium

This example considers the 1-D case of no initial intensity noise, $\delta I(0, \tau) = 0$, and frequency noise at $z = 0$ as given in Eq. 1.14. The power spectrum for the intensity $\delta I(z, \tau)$ in the high-average power, low-intensity regime can be found using Eq. 1.10a, and is given by $P_{\delta I}(z, \omega) = 4(1/\omega)^2 \Omega_\omega \Theta(\omega_B - |\omega|) \sin^2(\beta_2 \omega^2 z / 2)$. This can be seen as a transfer of frequency noise to intensity noise, a process which has been analyzed in the absence of nonlinear effects and demonstrated experimentally [25–27]. Depending on the value of ω_B, the intensity after propagation can fluctuate chaotically on scales much faster than the coherence time. One example of this is the system in Fig. 1.3 and 1.4, shown in Fig. 1.5 after $100\,\mathrm{m}$ propagation in air. At the wavelength $\lambda_0 = 1\,\mu\mathrm{m}$, the air exhibits normal group-velocity dispersion, i.e. $\beta_2 > 0$. This example corresponds to existing CW fiber laser systems in the kW-average power regime operating at $\lambda_0 = 1\,\mu\mathrm{m}$, [10], [28], [29]. For such systems, linewidths are due solely to noise, and depending on the power, may be as high as, $\Delta\omega / \omega_0 \sim 10^{-2}$.
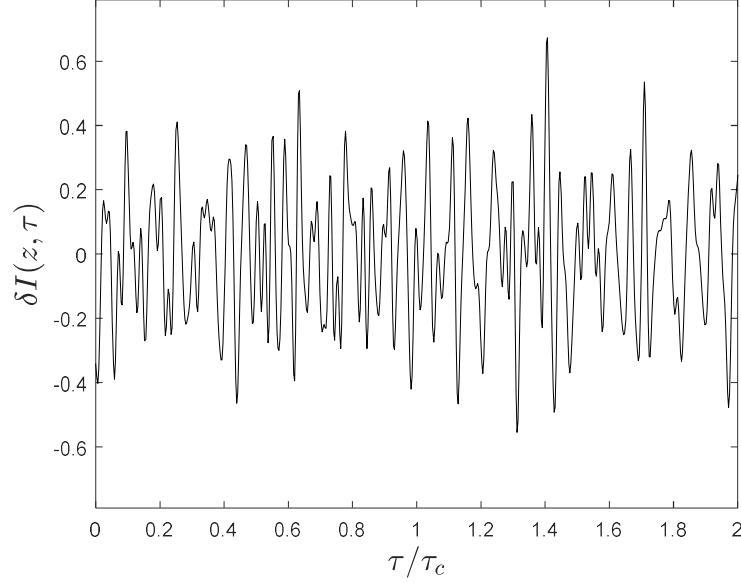
Figure 1.5. Intensity noise after propagation in air for 100 m, calculated using Eqs. (1.10a,b). The group velocity dispersion parameter has the value $\beta_2 = 0.17$ fs^2/cm. At $z = 0$ there was no intensity noise and the frequency noise was as described in Eq. 1.14. The numerical parameters are $\lambda_0 = 1$ μm, $\Delta\omega / \omega_0 = \Omega_\omega / \omega_0 = 10^{-3}$, $2\omega_B / \omega_0 = 10^{-1}$, $\omega_0 \Delta t = 19.2$, and $N_\tau = 2^{16}$. The average intensity is 1 kW/cm^2. Included are times $0 \le \tau / \tau_c \le 2$, where the coherence time is $\tau_c \approx 3$ ps. The intensity RMS value is $\sigma(\delta I) \equiv \langle \delta I^2 \rangle^{1/2} = 0.22$ after propagation.

This result agrees quantitatively with solution of the NLSE using a split-step Fourier method with the same input parameters and field.

1.3.3. Transfer of frequency noise to intensity noise in a nonlinear dispersive medium

For an arbitrary average intensity in 1-D, the spectrum of the intensity noise due to transfer of frequency noise, Eq. 1.14, can be found using Eq. 1.10a, and is
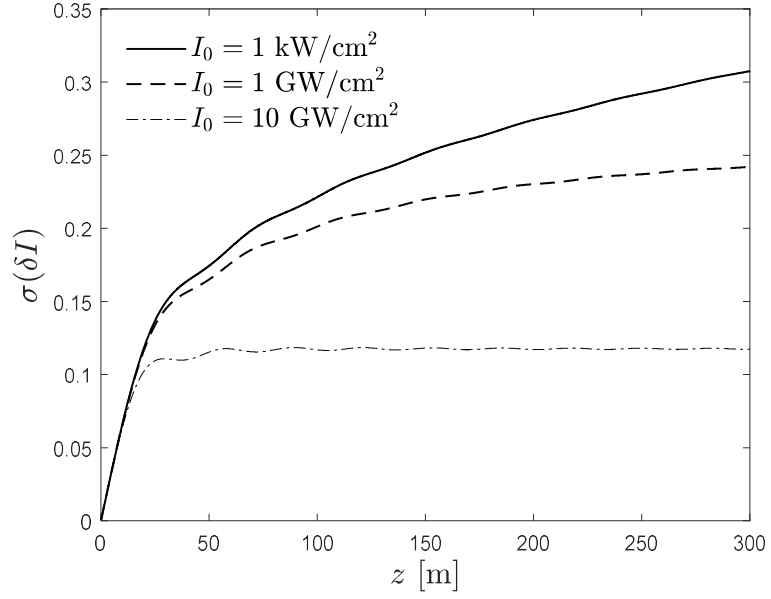
Figure 1.6. RMS value of the intensity noise $\sigma(\delta I)$ as a function of propagation distance for three values of laser intensity. Propagation parameters as in Table 1.1. Numerical parameters are $\lambda_0 = 1$ μm, $\Delta\omega / \omega_0 = \Omega_\omega / \omega_0 = 10^{-3}$, $2\omega_B / \omega_0 = 10^{-1}$.

$$P_{\delta I}(z, \omega) = \Omega_\omega \frac{\beta_2^2 \omega^2}{K^2(\omega)} \Theta\left(\omega_B - |\omega|\right) \sin^2\left(K(\omega) z\right). \tag{1.17}$$

As the beam intensity I_0 becomes large, so too does the value of $K^2 = K_0^2 / 4 + K_0 k_{NL}$.

As a result, the RMS value of the intensity noise which results from the transfer of noise

from the frequency, due to dispersive propagation (Fig. 1.5), decreases with increasing

intensity.

Through the Wiener-Khinchin theorem, [30], the power spectrum $P_F(\omega)$ of a

function F is related to its RMS value, $\sigma(F)$, by an integral over frequency space,

24

$\sigma^2(F) = \dfrac{1}{2\pi} \displaystyle\int_{-\infty}^{\infty} P_F(\omega)\,d\omega.$ Figure 1.6 shows the RMS intensity noise, $\sigma(\delta I)$, as a

function of the propagation distance z for several values of the average intensity and

wavelength $\lambda_0 = 1\ \mu\text{m}$. From Fig. 1.6, we see that as the intensity increases into the short-

pulse regime, $\sigma(\delta I)$ decreases, as the transfer of noise from the frequency to the

intensity is suppressed.

1.3.4. Spectral modification due to noise in a nonlinear dispersive medium

In the previous examples, the input intensity noise was $\delta I(0, \tau) = 0$. If, however,

the input intensity noise is described by Eq. 1.15 (Lorentzian noise), spectral broadening

can occur for the case of a short pulse, high-intensity laser. This broadening is due to self-

phase modulation, but is purely a noise-induced effect, and is independent of the

frequency spread/chirp due to the laser envelope. Figure 1.7 shows the laser spectral line

of a $\lambda_0 = 0.85\ \mu\text{m}$, $I_0 = 0.2\ \text{TW/cm}^2$ pulse after 3 km propagation through the

atmosphere.

In the example shown in Fig. 1.7, the initial beam is monochromatic, while the

fractional linewidth after propagating 3 km is $\Delta\omega / \omega_0 \sim 0.6 \times 10^{-3}$. As a comparison, the

transform-limited linewidth of a 500 ps pulse (corresponding to the numerical parameters

in Fig. 1.7) is $\Delta\omega / \omega_0 \sim 5 \times 10^{-6}$. For the same pulse and paramters, an estimate of the

fractional (envelope-induced) frequency shift due to propagation in a Kerr medium is

$\delta\omega_{Kerr} / \omega_0 \approx I_0 n_2 k_0 z / \tau_L \omega_0 = 10^{-3}$, where the pulse duration is $\tau_L = 500\ \text{ps}$. This suggests
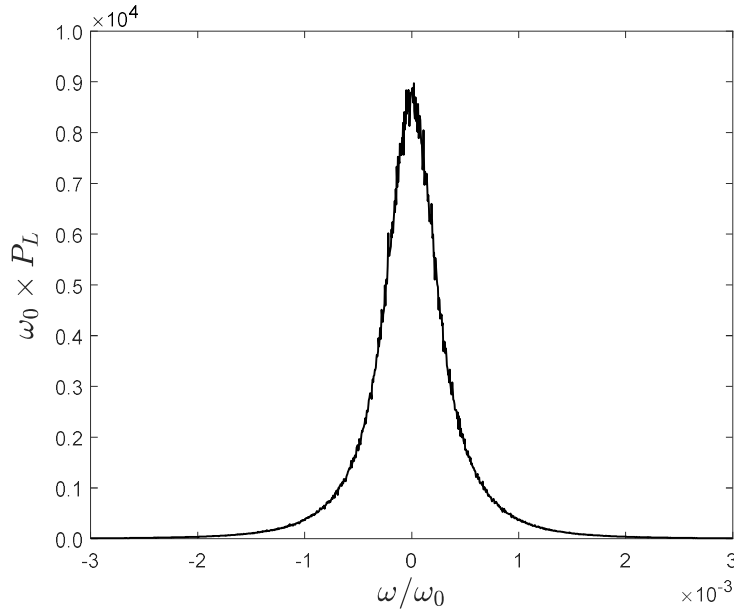
Figure 1.7. Laser spectral line $P_L(\omega)$ of a $\lambda_0 = 0.85$ μm, $I_0 = 0.2$ TW/cm^2 laser beam after 3 km propagation through the atmosphere, with only initial intensity noise as given in Eq. 1.15. Propagation parameters are given in Table 1.1. Numerical parameters are $\omega_0 \Delta t = 19.2$ and $N_\tau = 2^{16}$. The initial intensity noise had spectral width $\Omega_I / \omega_0 = 10^{-3}$ and $\sigma(\delta I) = 10^{-2}$.

that for the parameters in this example, the effects of nonlinear spectral broadening due to noise and due to a pulse's finite envelope may be comparable.

1.3.5. Longitudinal modulational instability

For 1-D longitudinal noise, if the group-velocity dispersion parameter β_2 is negative, the system in Eq. 1.10a,b is unstable, i.e., $K^2 < 0$, for $|\beta_2| \omega^2 < 4 k_{NL}$. In the presence of intensity noise, as per Eq. 1.15, and in the absence of initial frequency noise,
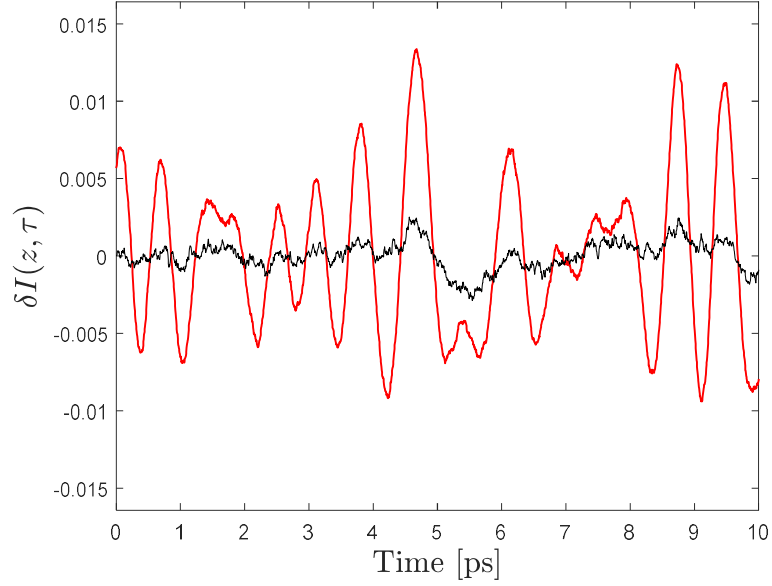
Figure 1.8. Shows the longitudinal modulational instability before (black) and after (red) 3 km propagation in atmosphere, with no input frequency noise. In this example, $\lambda_0 = 10.6$ μm and the average laser intensity is $I_0 = 5$ GW/cm^2. Propagation parameters are $n_2 = 4 \times 10^{19}$ cm^2/W and $\beta_2 = -0.3$ fs^2/cm. Numerical parameters are $\omega_0 \Delta t = 0.719$ and $N_\tau = 2^{18}$. The intensity noise before propagation was Lorentzian, with spectral width $\Omega_I / \omega_0 = 10^{-2}$ and RMS value $\sigma(\delta I) = 10^{-3}$.

the final intensity noise spectrum is $P_I(z, \omega) = P_I(0, \omega) \cos^2(K z)$, where

$$K(\omega) = (1/2)\sqrt{|\beta_2|\omega^2}\sqrt{|\beta_2|\omega^2 - 4k_{NL}}$$ may be purely real or purely imaginary. Figure

1.8 shows the instability for a 10.6 μm beam at $I_0 = 5$ GW/cm^2 in configuration space

before and after 3 km propagation in atmosphere.

Carbon dioxide laser pulses in the 10 μm regime have been produced with pulse

lengths of ~ 3 ps and peak intensities in the multi-Terawatt regime, and have been

proposed as candidates for directed energy applications [31], [32]. By comparison, the

27

intensity in our example is relatively modest. This is a strong indication that the interaction of dispersion and nonlinearity will be of great relevance to atmospheric propagation of laser pulses at these wavelengths, and that depending on noise levels in the individual pulses, disruptive instabilities may be seeded.

1.3.6. Saturation of the longitudinal modulational instability

Because saturation necessarily takes place in the non-perturbative regime, it cannot be simulated using Eqs. 1.10a,b. Instead, it is possible to use a split-step Fourier algorithm to solve the nonlinear Schrodinger equation, Eq. 1.4.

For our initial $\lambda_0 = 10.6$ μm pulse, we use a 100 ps $\sin^2$ envelope, peak intensity 10 GW/cm^2, modulating Lorentzian intensity noise with spectral width $\Omega_I / \omega_0 = 10^{-3}$ and RMS value $\sigma(\delta I) = 10^{-2}$. This pulse at z = 0 is then propagated through atmosphere using a split-step Fourier code solving Eq. 1.4, with the self-steepening and delayed Raman terms dropped. Atmospheric parameters are those given in Table 1.1. Figure 1.9a shows a 5 ps section of the pulse's peak at z = 0 km, z = 1 km and z = 2 km, while Figure 1.9b shows the same section at z = 3 km.
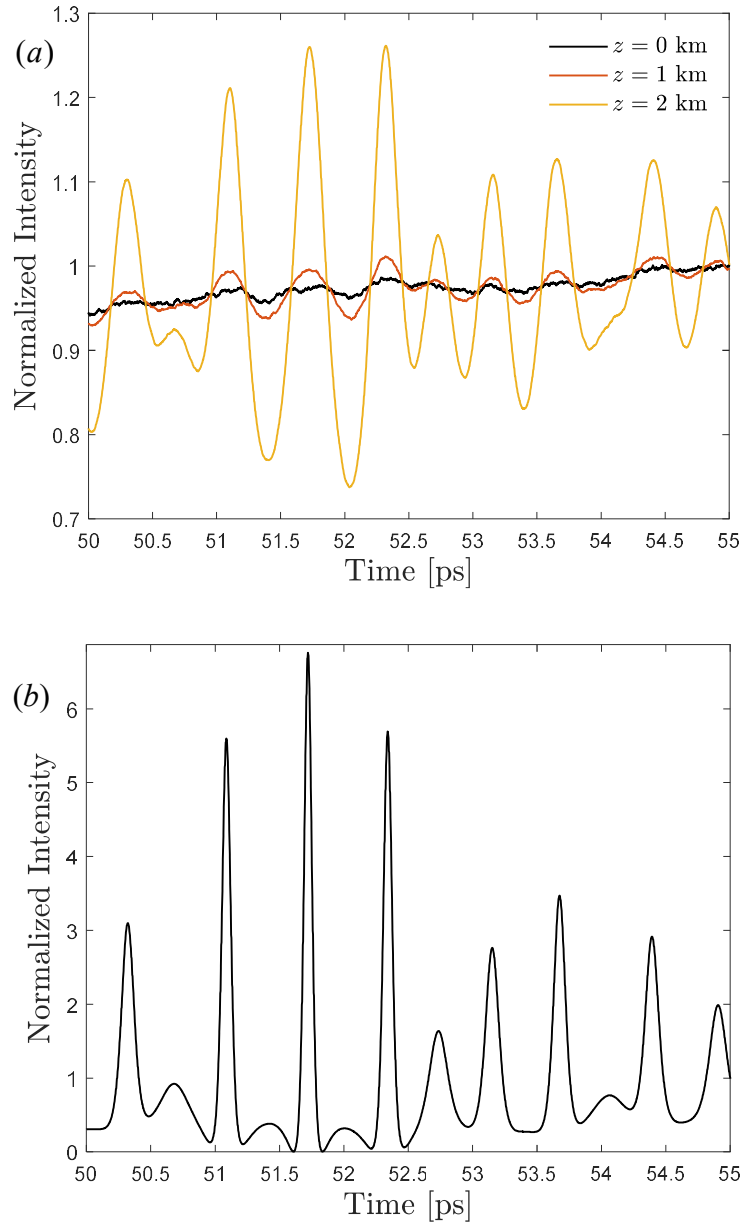
Figure 1.9. Shows intensity for a 5 ps section of a 100 ps, $\lambda_0 = 10.6\ \mu m$, $\sin^2$ pulse, normalized to the peak intensity 10 GW/cm^2, after propagation through atmosphere, parameters in Table 1.1. NLSE solved using split-step Fourier algorithm. Intensity given for (a) z = 0 km, 1 km, 2 km and (b) z = 3 km.
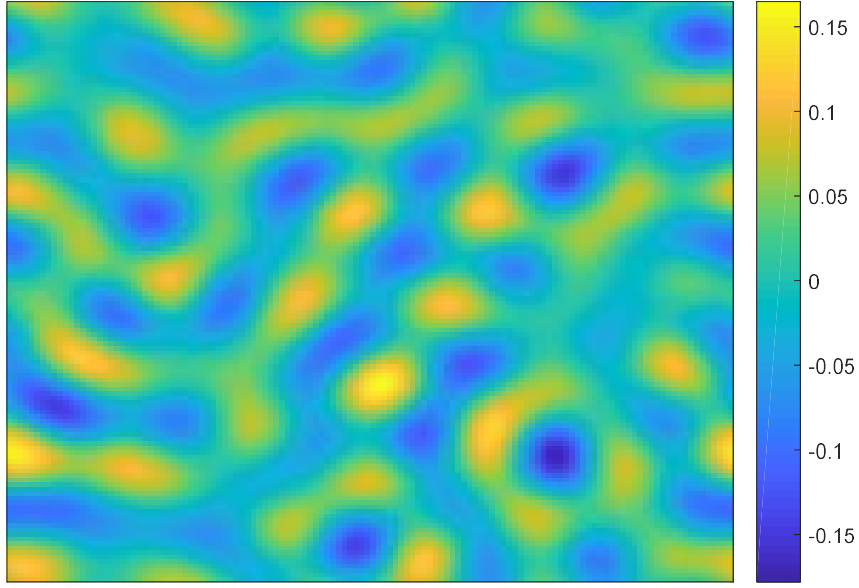
Figure 1.10. Shows growth of the modulational instability for the transverse intensity noise (given initially by Eq. 1.18) at $z = 200$ m. $N_x = N_y = 128$, $x_{max} = y_{max} = 5$ cm, $n_2 = 4 \times 10^{19}$ cm^2/W, $I_0 = 10^{10}$ W/cm^2, $\sigma(\delta I) = 10^{-3}$, $\lambda_0 = 0.85$ μm. The e-folding length $L_e = 1 / \mathrm{Im}(k_\perp)$ at the maximum growth rate is $L_e \approx 30$ m.

1.3.7. Transverse modulational instability

As an illustration of the effect of transverse noise in the initial intensity, we show growth of the transverse modulational instability. We represent the initial transverse intensity fluctuations as white noise,

$$\delta I(0, x, y) = \sum_{j, l=0}^{N_x/2, \, N_y/2} R_{j,l} \cos\left(k_{x,j} x + k_{y,l} y + \theta_{j,l} \right), \tag{1.18}$$

where $k_{x,j} = 2\pi j / N_x \Delta x$, $k_{y,l} = 2\pi l / N_y \Delta y$, $R_{j,l}$ are a set of normal random numbers with zero mean, and $\theta_{j,l}$ are uniform random numbers on the interval $[0, 2\pi]$. The dimensions of the simulation window are y_{max} and x_{max}, separated into an $N_x \times N_y$ grid, with grid point spacing Δx and Δy. Figure 1.10 shows the transverse modulational instability, where the intensity after propagation has been calculated using Eqs. 1.10a,b. This instability is the cause of the filamentation process which occurs when the laser power exceeds the critical focusing power P_{Kerr}. The number of filaments formed is roughly equal to the laser power divided by P_{Kerr}, as discussed in Section 1.2.2.

1.4. Discussion

In this chapter, we have studied the effect of laser noise on the propagation of laser radiation in dispersive and nonlinear media. We used a laser propagation equation which includes nonlinear Kerr effects, group velocity dispersion, the delayed Raman response, and optical self-steepening. The laser beams under consideration have noise components in the intensity and frequency. Our propagation equations are first-order in the intensity and frequency fluctuations. We also analyzed the saturation of the longitudinal modulational instability and found that saturation occurs without requiring ionization to arrest growth.

We chose a few examples to study analytically and numerically. Computational examples were carried out both for high-intensity, short pulse lasers having a wavelength $\lambda_0 = 0.85$ μm and $\lambda_0 = 10.6$ μm, for which nonlinear and dispersion effects are

31

important, and for high-average power lasers having wavelength $\lambda_0 = 1\,\mu\text{m}$, for which nonlinear effects can be neglected but dispersion can play an important role.

The examples include simulations of the transverse and longitudinal modulational instabilities (for which a more complete dispersion relation is derived in Appendix 1.A). For media with anomalous group-velocity dispersion (e.g. 10.6 μm radiation in humid air) pulse parameters exist which may result in soliton behavior, allowing a pulse to propagate long distances without significant reduction in intensity (Appendix 1.B). In addition, we examined the conversion of frequency noise into intensity noise for lasers propagating in the atmosphere. We found that the transverse and longitudinal noise can be transferred between the phase and intensity fluctuations, an effect which may have important implications for adaptive optics applications. For example, if a beam initially has no intensity fluctuations, but has a nonzero linewidth due to phase noise, after propagation, intensity fluctuations may grow to be of order unity (Fig. 1.5). We also showed that when the Kerr nonlinearity is included, this conversion effect can be mitigated for high intensity lasers. Finally, we demonstrated noise-induced spectral broadening for a short laser pulse.

Appendix 1.A: Full dispersion relation

In deriving our pulse propagation equation, several assumptions were made. First, the group velocity was assumed to be approximately equal to the phase velocity, allowing some cancellations to be made. In addition, a second derivative term in z was dropped. For the parameters in our examples, these approximations proved to be valid.

However, a more complete dispersion relation can be derived without some of these approximations.

Beginning with Eq. 1.2, and keeping only the second-order dispersion term, proportional to β_2, the pulse propagation equation is

$$
\nabla_\perp^2 \hat{E} + \frac{\partial^2 \hat{E}}{\partial z^2} + 2ik_0\left(1 + \frac{i}{v_g\, k_0}\frac{\partial}{\partial \tau}\right)\frac{\partial \hat{E}}{\partial z}
$$

$$
- k_0\,\beta_2\,\frac{\partial^2 \hat{E}}{\partial \tau^2} + 4\pi\frac{\omega_0^2}{c^2}\left(1 + \frac{i}{\omega_0}\frac{\partial}{\partial \tau}\right)^2 \hat{P}_{NL} = 0,
$$

(1.A.1)

where the nonlinear polarization is defined in Section 1.2. The electric field is perturbed about a steady-state solution, $\hat{E} = E_0(z) + \delta E(\mathbf{r}, \tau)$, where $E_0(z)$ is defined by the equation $\partial^2 E_0 / \partial z^2 + 2ik_0\partial E_0 / \partial z + 2k_0 k_{NL} E_0 = 0$, which has the solution

$E_0 = A_0 \exp\left(i\bar{k}_{NL} z\right)$, where $\bar{k}_{NL} = k_0\left(\sqrt{1 + 2k_{NL}/k_0} - 1\right) \approx k_{NL}\left(1 - k_{NL}/2k_0 + ...\right)$ for a

forward-propagating wave. Keeping first-order terms in the perturbation, and dropping the small $(\partial / \omega_0\partial \tau)^2$ term, the equation for δE is

$$
\nabla_\perp^2\, \delta E + \frac{\partial^2 \delta E}{\partial z^2} + 2ik_0\left(1 + \frac{i}{v_g\, k_0}\frac{\partial}{\partial \tau}\right)\frac{\partial \delta E}{\partial z}
$$

$$
- k_0\,\beta_2\,\frac{\partial^2 \delta E}{\partial \tau^2} + 2k_0\gamma_{NL}\left(1 + \frac{2i}{\omega_0}\frac{\partial}{\partial \tau}\right)(2I_0\,\delta E + \kappa_0\, E_0 E_0\,\delta E^*) = 0
$$

(1.A.2)

Setting $\delta E(r,\tau) = \delta A(r,\tau)\exp(i\bar{k}_{NL} z)$, we obtain

33

$$\left(\nabla_\perp^2 + \frac{\partial^2}{\partial z^2} - k_0 \beta_2 \frac{\partial^2}{\partial \tau^2} \right) \delta A + 2 i k_0 \left(1 + \frac{i}{v_g k_0} \frac{\partial}{\partial \tau} \right) \frac{\partial \delta A}{\partial z}$$

$$+ 2 k_0 k_{NL} \left[\delta A + \delta A^* + \frac{4i}{\omega_0} \left(1 - \frac{\omega_0}{4 v_g k_0} \right) \frac{\partial \delta A}{\partial \tau} + \frac{2i}{\omega_0} \frac{\partial \delta A^*}{\partial \tau} + \frac{i}{k_0} \frac{\partial \delta A}{\partial z} \right] = 0.$$

(1.A.3)

Defining $\delta A = \delta A_R + i \delta A_I$, where $\delta A_R = \mathrm{Re}[\delta \hat{A}_R \exp(i(\mathbf{k} \cdot \mathbf{r} - \omega \tau))]$,

$\delta A_I = \mathrm{Re}[\delta \hat{A}_I \exp(i(\mathbf{k} \cdot \mathbf{r} - \omega \tau))]$, and $\mathbf{k} \cdot \mathbf{r} = k_x x + k_y y + k_z z$ leads to a system of

equations for $\delta \hat{A}_R$ and $\delta \hat{A}_I$,

$$\left(k_\perp^2 + k_z^2 - k_0 \beta_2 \omega^2 + 2 k_z \frac{\omega}{v_g} - 4 k_0 k_{NL} \right) \delta \hat{A}_R$$

$$+ 2 i k_0 \left(\left(1 + \frac{k_{NL}}{k_0} \right) k_z - k_{NL} \left(2 - \frac{\omega_0}{v_g k_0} \right) \frac{\omega}{\omega_0} \right) \delta \hat{A}_I = 0,$$

$$\left(k_\perp^2 + k_z^2 - k_0 \beta_2 \omega^2 + 2 \frac{\omega}{v_g} k_z \right) \delta \hat{A}_I$$

(1.A.4)

$$- 2 i k_0 \left(\left(1 + \frac{k_{NL}}{k_0} \right) k_z - k_{NL} \left(6 - \frac{\omega_0}{v_g k_0} \right) \frac{\omega}{\omega_0} \right) \delta \hat{A}_R = 0.$$

Combining Eqs. 1.A.4 gives the dispersion relation,

$$4 k_0^2 \left[\left(1 + \frac{k_{NL}}{k_0} \right) k_z - k_{NL} \left(2 - \frac{\omega_0}{v_g k_0} \right) \frac{\omega}{\omega_0} \right] \left[\left(1 + \frac{k_{NL}}{k_0} \right) k_z - k_{NL} \left(6 - \frac{\omega_0}{v_g k_0} \right) \frac{\omega}{\omega_0} \right]$$

$$- \left(k_\perp^2 + k_z^2 - k_0 \beta_2 \omega^2 + 2 k_z \frac{\omega}{v_g} - 4 k_0 k_{NL} \right) \left(k_\perp^2 + k_z^2 - k_0 \beta_2 \omega^2 + 2 \frac{\omega}{v_g} k_z \right) = 0.$$

(1.A.5)

Appendix 1.B: Laser envelope

The envelope $\hat{E}(r, z, \tau)$ of a laser pulse may be approximated as Gaussian both transversely and longitudinally, i.e.

$$\hat{E}(r, z, \tau) = A(z) e^{i\theta(z)} e^{-[1+i\alpha(z)]r^2/R^2(z)} e^{-[1+i\beta(z)]\tau^2/T^2(z)}. \tag{1.B.1}$$

and the peak intensity is $I(z) = \kappa_0 |\hat{E}|^2$. By substituting this into the propagation equation, Eq. 1.4, and expanding to second-order in r and τ, the dynamics of the pulse duration T and spot size R, as well as the curvature α and β, which is proportional to the chirp, can be shown to be given by [11]

$$
\begin{aligned}
\frac{\partial^2 R}{\partial z^2} &= \frac{4}{k_0^2 R^3}\left(1 - \frac{E_0}{\tilde{P}_{Kerr}}\frac{1}{T}\right), \\
\frac{\partial^2 T}{\partial z^2} &= \frac{4\beta_2}{T^2}\left(\frac{E_0}{k_0\tilde{P}_{Kerr}}\frac{1}{R^2} + \frac{\beta_2}{T}\right), \\
\alpha(z) &= -\frac{k_0 R}{2}\frac{\partial R}{\partial z}, \\
\beta(z) &= \frac{T}{2\beta_2}\frac{\partial T}{\partial z},
\end{aligned}
\tag{1.B.2}
$$

where the conserved pulse energy is $E_0 = \pi R^2 T I / 2$, and the critical power is

$\tilde{P}_{Kerr} = \lambda_0^2 / 8\pi n_0 n_2$. From this, we can find conditions for the pulse to be a soliton, i.e.

$\partial R(z) / \partial z = 0, \ \partial T(z) / \partial z = 0$,

$$T_s = \frac{E_0}{\tilde{P}_{Kerr}},$$

$$R_s = \frac{1}{\sqrt{|\beta_2|k_0}} \frac{E_0}{\tilde{P}_{Kerr}}. \tag{1.B.3}$$

where the group-velocity dispersion must be anomalous, i.e. $\beta_2 < 0$.

These conditions can also be arrived at by analysis of the dispersion relation in Eq. 1.12. First, we recognize that a pulse which is finite in the longitudinal and transverse directions cannot seed an instability at frequencies smaller than $\omega_{min} \sim 2/T$ and transverse wavenumbers smaller than $k_{\perp,min} \sim 2/R$. For stability (no self focusing) the growth rate $\Gamma = \text{Im}[k]$ must be zero for all $|k_\perp| > k_{\perp,min}$ and $|\omega| > \omega_{min}$, a condition which can only be satisfied for $\beta_2 < 0$. Additionally, for soliton behavior, the minima ω_{min} and $k_{\perp,min}$ should be situated at the edge of the region of stability, leading to the condition $k_{\perp,min}^2 + |\beta_2|\omega_{min}^2 k_0 = 4k_0 k_{NL}$. After substitution, we find

$T_s^2 - (2E_0 / P_{Kerr}')T_s + |\beta_2|k_0 R_s^2 = 0$, where $P_{Kerr}' = \lambda_0^2 / 4\pi n_0 n_2$. From this, and the assumption that the soliton spot size and pulse length should be defined unambiguously, we recover the previous conditions, Eqs. 1.B.3.

The soliton solution can be analyzed for envelope stability by perturbing the equations for $T(z)$ and $R(z)$ about the soliton conditions T_s and R_s, and assuming the perturbations go like $\sim \exp(ikz)$. In this case, the wavenumber k follows the equation

$$k^2\left(k^2 - \frac{4\beta_2^2}{T_0^4}\right) = \frac{32}{k_0^2} \frac{\beta_2^2}{T_0^4 R_0^4}, \tag{1.B.4}$$

with stable roots $k = \pm\sqrt{8}\,|\beta_2|/T_0^2$ and unstable root $k = \pm\,2i\,|\beta_2|/T_0^2$.

The presence and dynamics of solitons in air at $\lambda_0 = 10.6$ µm ($P_{Kerr} \approx 450$ GW) have been analyzed numerically in detail elsewhere [33], however some basic estimates of their characteristics can be calculated from the analysis in this appendix. For a 1 ps pulse, the pulse energy should be $E_0 \approx 0.45$ J, and the spot size should be $R_0 \sim 0.2$ m. At these parameters, the e-folding length for perturbations to the spot size and pulse length is $L_e \sim 10$ km.

Chapter 2. Remote detection of radioactive material using optically induced air breakdown ionization

2.1. Introduction

Sources of radioactivity range from terrestrial, to cosmogenic and man-made [34]. In general, radioactive material emits ionizing radiation, for example gamma rays, which ionize the surrounding air, producing high-energy electrons which cascade down to low energy, thermal electrons [35]. These low energy electrons rapidly attach to oxygen molecules forming O_2^- ions. At ambient levels of radiation, the density of free electrons is much less than the density of molecular oxygen ions [36].

Remote radiation detection concepts have been proposed based on high-power terahertz (THz) radiation pulses that induce avalanche (collisional) air breakdown in the vicinity of the radioactive material [37], [38]. Here, a THz pulse is focused near the radioactive material. In order to initiate avalanche breakdown at least one electron needs to be in the optical volume for many ionization times. At ambient levels of radioactivity the free (seed) electron density in the optical volume will be small so that the probability of avalanche breakdown is small, i.e., the average breakdown time is long, or breakdown does not occur, depending on the duration of the THz pulse. However, in the presence of radioactive material the probability of breakdown occurring is higher because the density
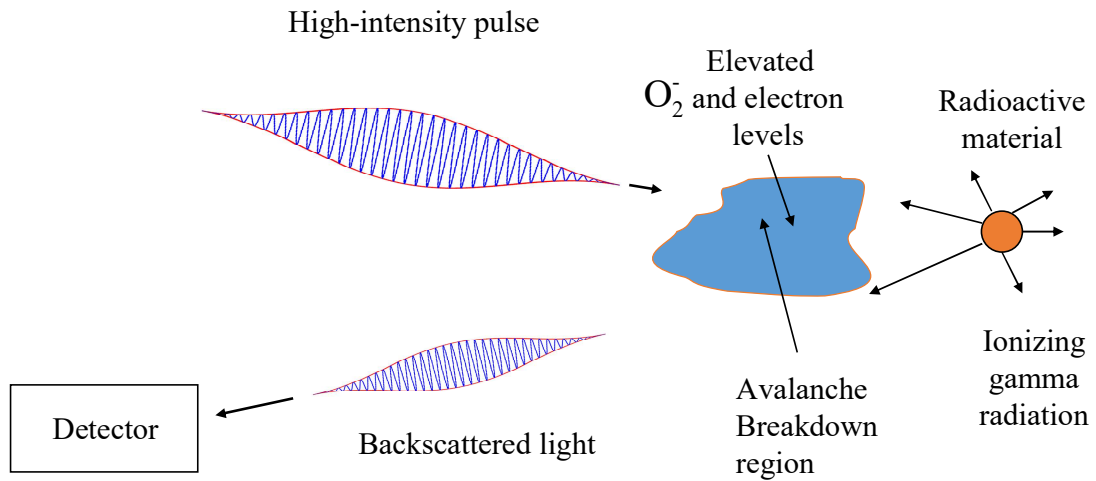
Figure 2.1. Schematic of the detection mechanism.

of free electrons available to seed the avalanche process is higher, i.e., the average

breakdown time is shorter. A variation in spark breakdown probability and therefore

average time delay is an indication of a difference in surrounding radioactivity.

Another proposed concept for the remote detection of radioactivity consists of

photo-detaching electrons from the O_2^- ions in order to enhance the level of seed

electrons in the optical volume for the avalanche breakdown process [39]. In this concept,

a single, high-power IR laser beam is used for both the photo-ionizing and avalanche

ionizing beams (Fig. 2.1). In this bistatic detection concept the electromagnetic signature

for the presence of radioactive material is a frequency modulation on a probe beam

caused by the temporally increasing electron density [40]. A previous paper [2] analyzed

a specific example of remote detection, using a low-intensity photo-detaching laser pulse

($\lambda = 1\,\mu\text{m}$) to produce seed electrons, and a CO_2 laser ($\lambda = 10.6\,\mu\text{m}$) to induce avalanche air breakdown in the vicinity of radioactive materials.

In the present analysis, in addition to calculating the increase in the density of negative ions due to the presence of radioactivity, we will perform a more general analysis of detection through ion-seeded avalanche breakdown. Using a system of coupled rate equations, we derive the avalanche breakdown threshold intensity for a range of laser frequencies, as well as the breakdown equilibrium temperature and ionization rate for several specific frequencies. We also analyze the ion density and laser pulse parameter requirements both for detection by breakdown time delay statistics and by single-pulse breakdown time delay measurement.

2.2. Ion-seeded avalanche breakdown

2.2.1. Radioactive electron generation and negative ion formation

Upon disintegration, many types of radioactive nuclei emit ionizing radiation which, through a Compton scattering process (gammas), generate high-energy electrons that cascade down in energy. Due to its high electron affinity the majority of these ions are oxygen molecules, and at sea level are predominantly O_2^- rather than O^-. An example of this process is the disintegration of Cobalt-60 (^{60}Co). Upon each disintegration of a ^{60}Co nucleus, two gammas are emitted, each with an energy of $\approx 1\,\text{MeV}$. The MeV gammas have a mean-free-path in air of ~130 m. Each of these gammas produce ~30,000 electrons which eventually recombine and/or form negative oxygen ions [35].

As a result of cosmic rays, radioactive substances in the ground and air, the ambient ionization rate is $Q_{rad} \approx 10 - 30$ cm^{-3}s^{-1} [34]. The presence of additional radioactive material can significantly increase the radioactive ionization rate to $(1+\alpha_{rad})Q_{rad}$ where $\alpha_{rad} \gg 1$ is the enhancement factor resulting from the additional radioactive material. For example, 50 cm from 10 mg of ^{60}Co (a dirty bomb may contain many hundreds of mg), the enhancement factor in air can be as high as $\alpha_{rad} \sim 10^6$ [39]. In general, for an unshielded, localized source of gammas, the radioactivity enhancement factor falls off like $\exp(-R/L_\gamma)/R^2$, where R is the distance from the source and L_γ is the effective range of the gammas.

2.2.2. Electron, ion, and electron energy density rate equations

The electron density, ion density and electron temperature are modeled using the following rate equations [2],

$$\frac{\partial n_e}{\partial t} = \left(1+\alpha_{rad}\right)Q_{rad} + \nu_{photo}\, n_- + \nu_{coll}\, n_e - \nu_a\, n_e - \beta_{e+}\, n_+\, n_e + 0.8\beta_n n_n n_-,$$

$$\frac{\partial n_-}{\partial t} = -\nu_{photo}\, n_- + \nu_a\, n_e - \beta_\pm\, n_+\, n_- - \beta_n\, n_n\, n_-, \qquad (2.1a-2.1c)$$

$$\frac{3}{2}\frac{\partial(n_e T_e)}{\partial t} = \langle \mathbf{J}\cdot\mathbf{E} \rangle - n_e \varepsilon_{loss},$$

where n_e is the electron density, n_- is the negative ion density (taken to be O_2^- at sea level), $n_+ = n_e + n_-$ is the positive ion density, $n_n = n_{n0} - n_+ - n_-$ is the neutral density (the ambient density is taken to be $n_{n0} = 2.7\times10^{19}$ cm^{-3}), ν_{photo} is the photo-detachment

rate, ν_{coll} is the collisional ionization rate, η is the electron attachment rate, β_{e+} is the electron-ion dissociative recombination rate, β_n is the negative ion detachment rate due to collisions with molecular nitrogen, $\beta_{\pm}$ is the ion-ion recombination (mutual neutralization) rate, T_e is the electron temperature in eV ($T_e[\text{eV}] = k_B T_e[^\circ\text{K}]$), $\langle \mathbf{J} \cdot \mathbf{E} \rangle$ is the Ohmic (inverse Bremsstrahlung) heating rate, and ε_{loss} is the electron energy loss rate in air. These air chemistry rates and collisional ionization rates are discussed in Appendices 2.A and 2.B and are in general functions of electron temperature. This model assumes a continuum of electrons and ions, an assumption which will be explored in a later section.

2.2.3. Ion density elevation due to radioactivity

In the absence of laser radiation, the background densities of electrons and negative ions reach a steady state, determined by the surrounding level of radioactivity, which is contained in the first term on the right-hand side of Eq.(2.1a), i.e., $(1 + \alpha_{rad}) Q_{rad}$. The steady state electron and negative ion densities can be estimated to be given by

$n_e \approx (\beta_n n_{n0} / \nu_a)((1 + \alpha_{rad}) Q_{rad} / \beta_{\pm})^{1/2}$ and $n_- \approx ((1 + \alpha_{rad}) Q_{rad} / \beta_{\pm})^{1/2}$ [39]. In steady state, the negative ion density is solely determined by the ion-ion recombination rate and the level of radioactivity. The ratio of the electron to ion density in the steady state is

$n_e / n_- \approx \beta_n n_n / \eta \sim 10^{-6}$. For typical atmospheric parameters, the ion density in the

presence of a radioactive material is $n_i \sim 10^3 \text{ cm}^{-3} \times (1 + \alpha_{rad})^{1/2}$. This is consistent with experimental measurements of the ion background, with $\alpha_{rad} = 0$ [36].

2.2.4. Single- and two-photon detachment of O_2^-

The electron affinity (ionization potential) for O_2^- has been measured to be approximately 0.45 eV [41]. For laser photon energies greater than this, $\lambda < 2.7$ μm, photo-detachment occurs via a single-photon absorption process. The detachment rate is $\nu_{photo} = \sigma_{pd} I_0 / \hbar\omega$, where σ_{pd} is the cross-section for photo-detachment, I_0 is the incident laser intensity, and $\hbar\omega$ is the photon energy. The cross-section σ_{pd} has been measured experimentally for photon energies greater than 0.5 eV, and the data points fit to a theoretical curve [42],

$$\sigma_{pd} = \hbar\omega(\hbar\omega - E_0)^{3/2} \left[A_0 + A_1(\hbar\omega - E_0) + ... \right], \tag{2.2}$$

where the fitting parameters are $E_0 = 0.15$ eV, $A_0 = 0.370 \times 10^{-18}$ cm^2 eV$^{-5/2}$, and $A_1 = -0.071 \times 10^{-18}$ cm^2 eV$^{-7/2}$. For $\lambda = 1.06$ μm, the photo-detachment rate is $\nu_{photo}[\text{s}^{-1}] = 1.9\, I_0\ [\text{W/cm}^2]$.

The cross-section for two-photon detachment of O_2^- has not been measured experimentally, and the details of the process are not well-understood, however an approximate theoretical formula has been calculated for the specific case of $\lambda = 5.5$ μm, with $\nu_{photo}[\text{s}^{-1}] \approx 10^{-12}\, I_0^2\ [\text{W/cm}^2]$ [43].

2.2.5. Laser-induced avalanche breakdown

The basic theory of the avalanche breakdown of air in a laser field is well documented [44]. When a population of electrons is illuminated by a laser pulse which has an intensity greater than a threshold intensity I_{th}, free electrons are accelerated and collisionally ionize molecules at a rate greater than the rate of attachment. The breakdown threshold intensity can vary greatly depending on atmospheric conditions, laser pulse parameters, etc. [45], but can be approximated by finding the conditions in Eq. 2.1 for which ionization overcomes electron losses due to attachment, $\partial n_e / \partial t \approx \nu_{coll} n_e - \nu_a n_e > 0$. Because the collisional ionization rate and attachment rate are functions of the electron temperature, this equation and Eq. 2.1c must be solved self-consistently.

In the presence of a laser field, the electron energy density, $3n_e T_e / 2$, increases due to resistive heating at an average rate $\langle \mathbf{J} \cdot \mathbf{E} \rangle$ and decreases due to various inelastic cooling processes, including ionization, at a rate $n_e \varepsilon_{loss}$ (Appendix 2.A). If we assume weak ionization, $n_n \approx n_{n0} = 2.7 \times 10^{19}$ cm^{-3}, and that the electron density is an exponential function of time, i.e., $n_e(t) = n_e(0) \exp(\nu_{ion} t)$ [45], with $\nu_{ion} \approx \nu_{coll} - \nu_a$, then the electron temperature (from substituting our expression for $n_e(t)$ into Eq. 2.1c) can be shown to reach a steady-state, with

$$\frac{\partial T_e}{\partial t} = \frac{2}{3} \left(\langle \mathbf{J} \cdot \mathbf{E} \rangle / n_e - \varepsilon_{loss} \right) - \nu_{ion} T_e = 0 . \tag{2.3}$$
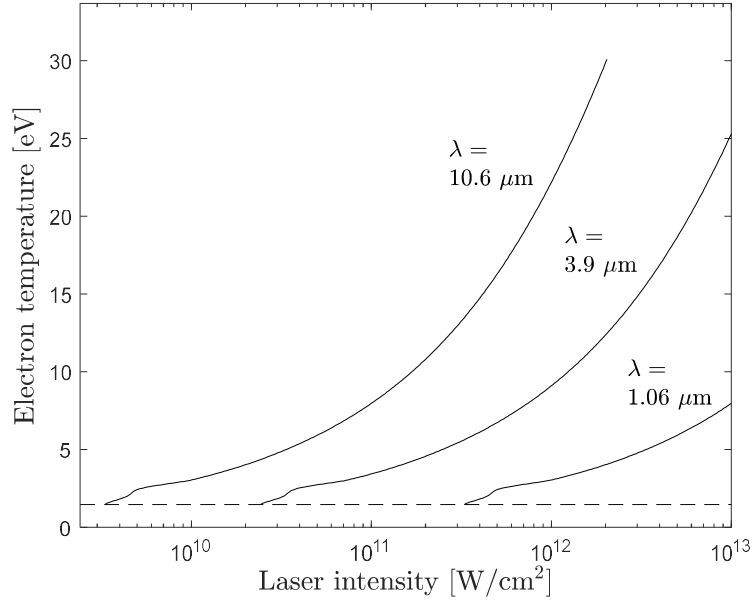
Figure 2.2. Steady-state breakdown temperature as a function of laser intensity for several laser wavelengths. These were calculated from Eq. 2.3, using the rates in Appendices 2.A and 2.B. The dotted line shows the breakdown threshold temperature $T_{th} = 1.47$ eV.

It should be noted that the expression $\langle \mathbf{J} \cdot \mathbf{E} \rangle / n_e$ does not depend on the electron density.

From this model, we can derive a theoretical breakdown threshold intensity in clean air for CW, 1-D laser pulses. For the rates given in Appendices 2.A and 2.B, the net ionization rate $\nu_{ion}(T_e)$ has a zero at $T_{th} = 1.47$ eV. For the electron density to increase, the steady-state temperature for a given intensity and wavelength must be greater than T_{th}. From Eq. 2.3, this is equivalent to stating that the intensity must be greater than

$$I_{th}[\text{W/cm}^2] = 3.69 \times 10^{11} \ \lambda^{-2}, \tag{2.4}$$
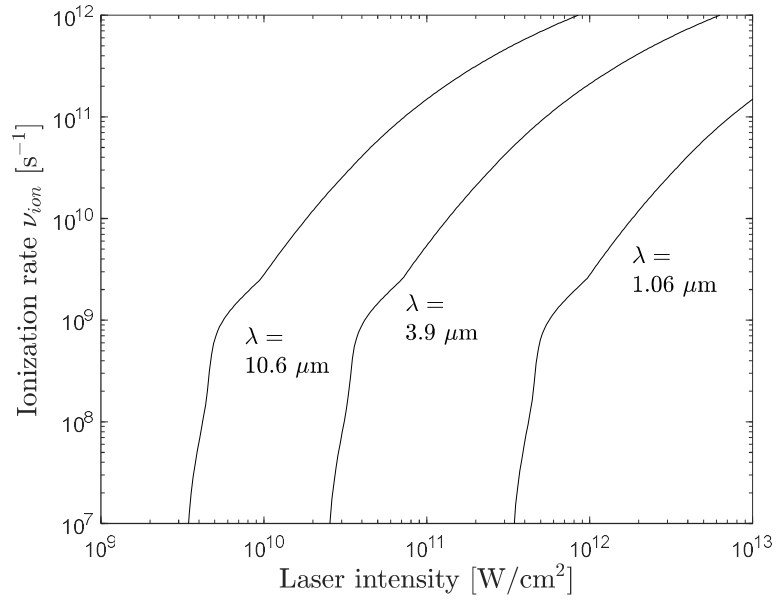
Figure 2.3. Ionization rate as a function of laser intensity, evaluated at the steady-state temperature during breakdown, shown for several values of the laser wavelength.

where the wavelength is in μm. This expression is in good agreement with previous theoretical and experimental determinations of the air breakdown threshold intensity.

The steady state breakdown temperature $T_{ss}(I_0, \lambda)$ calculated numerically from Eq. 2.3 is shown in Fig. 2.2 as a function of intensity for several values of the laser wavelength. These temperatures can be used to calculate the rate of ionization for the majority of the breakdown process, $\nu_{ion}\left(T_{ss}(I_0, \lambda)\right)$, shown in Fig. 2.3.
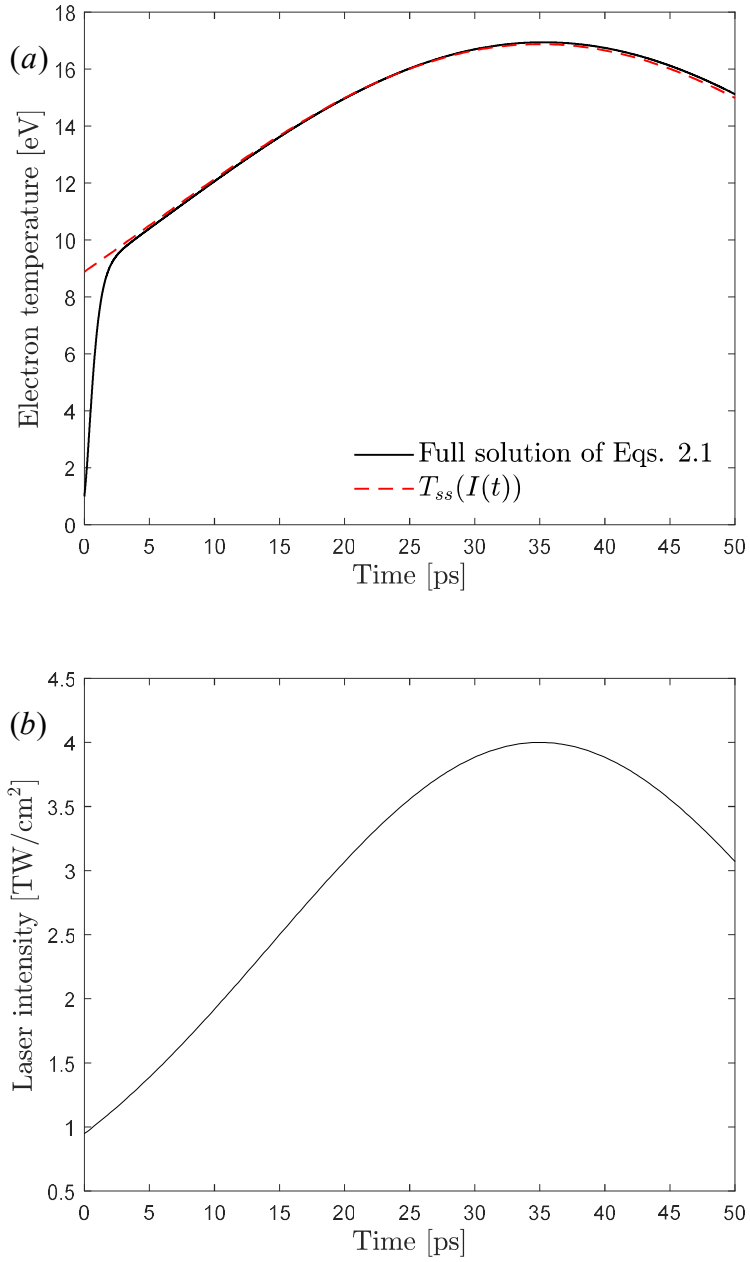
Figure 2.4. Electron temperature (a) during avalanche breakdown for a laser pulse, $\lambda = 3.9\ \mu m$, which is Gaussian in time (b). The red, dashed curve shows the calculated steady-state breakdown temperature for the given wavelength and intensity profile, while the solid curve shows the full numerical solution of Eq. 2.1a-c. The initial electron density was 10^4 cm^{-3}.

2.2.6. Breakdown temperature for time-dependent intensities

If the laser intensity is not constant, the assumptions made in deriving the steady-state avalanche breakdown temperature are not valid. However, if the intensity changes slowly compared to the time required for the temperature to equilibrate, then the calculated intensity-dependent temperature and ionization rate, Figs. 2.2 and 2.3, may be used. An example of avalanche breakdown driven by a Gaussian pulse, $\lambda = 3.9 \ \mu m$, is shown in Fig. 2.4a. The time-dependent laser intensity is shown in Fig. 2.4b.

It can be seen from Fig. 2.4 that the difference between the temperatures calculated by the two methods is very small for these parameters, after an initial equilibration time of a few picoseconds.

2.2.7. Breakdown delay time in the continuum model

We now make the assumption that our initial electron density $n_e(0)$ is due to the complete photo-detachment of the negative ions, so that $n_e(0) = n_{i0}\left(1 + \alpha_{rad}\right)^{1/2}$, where the ambient background ion density is taken to be $n_{i0} \sim 10^3 \ cm^{-3}$. If a low-intensity laser pulse is used to detach the electrons before a subsequent high-intensity pulse drives an avalanche breakdown [2], the second pulse may be of any wavelength. If, instead, the high-intensity heating pulse is also photo-detaching, this requires the photo-detachment term in Eq. 2.1a to be much greater than the collisional ionization term, which may place constraints on the wavelength, intensity and pulse duration.
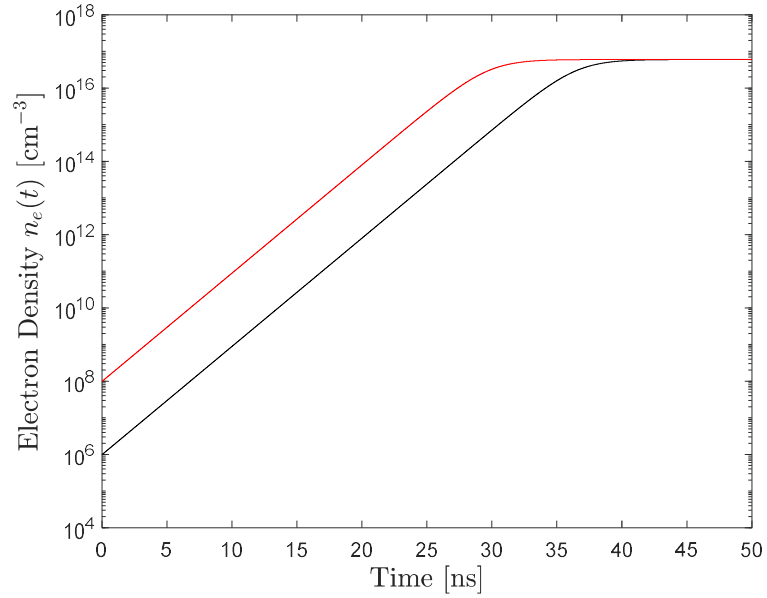
Figure 2.5. Electron density during breakdown, with $I_0 = 5 \times 10^9$ W/cm^2 and $\lambda = 10.6$ μm. The black curve had an initial electron density of $n_1(0) = 10^6$ cm^{-3} while the red curve had $n_2(0) = 10^8$ cm^{-3}.

For an exponential electron density with a constant rate, $n_e(t) = n_e(0) \exp(v_{ion} t)$, the time required to reach the electron density n_{bd} is $\tau_{bd} = \ln\left(n_{bd} / n_e(0)\right) / v_{ion}$. The total ionization rate is a function of the steady-state breakdown temperature, Figs. 2.2 and 2.3. For a fixed intensity and wavelength, the breakdown time is only a function of the radioactivity enhancement factor α_{rad}, and can therefore be used as a signature for the presence of radioactivity. This can be accomplished by comparing measurements at two nearby locations, one of which is the location in question.

As an example, consider a 50 ns, $\lambda = 10.6\ \mu\text{m}$ square laser pulse of intensity $I_0 = 5 \times 10^9$ W/cm^2 focused on an area 2.5×10^{-3} cm^2 (pulse energy ~ 0.5 J). The steady-state breakdown electron temperature for this intensity is 2.42 eV, and the corresponding total ionization rate is $v_{ion} = 6.5 \times 10^8$ s^{-1}. We will assume that all ions have been photo-detached by a previous pulse, so that a seed electron population with $n_1(0) = 10^6$ cm^{-3} is present in one remote location, and another with $n_2(0) = 10^8$ cm^{-3} is present in a second location near enough to the first so that all atmospheric variables are identical. The difference in breakdown times is $\tau_1 - \tau_2 = \ln(n_2/n_1)/v_{ion} = 7$ ns, which is readily measureable (Fig. 2.5).

2.2.8. Breakdown from one seed electron

If an avalanche breakdown ionization is seeded by a single electron, by the time the electron density reaches a detectable level, the plasma will occupy a finite volume due to electron diffusion surrounding the original location of the seed electron. When there are multiple seed electrons in the focal volume of the laser pulse, if the distance between seed electrons is too large (i.e. the density is too small), the breakdown plasma volumes will not overlap, and the time required for the plasma to reach a detectable level will not be a function of seed electron density and, in turn, level of radioactivity.

So far, our model has assumed a continuum of ions and electrons, in which the density of seed electrons is high enough that the electron density becomes continuous early in the avalanche breakdown ionization process. In this case, the breakdown time

can be used as a signature of radioactive ionization, as discussed in the previous section's example. The continuum assumption for ions and electrons may reasonably be used to model this detection method if the radius δ of the plasma volume, $V \approx 4\pi\delta^3/3$, resulting from an avalanche breakdown seeded by a single electron is much greater than the mean distance between seed electrons, i.e., $\delta \gg n_e(0)^{-1/3}$.

To approximate the dynamics of an avalanche breakdown ionization seeded by a single electron, we model the total electron number as $N_e(t) \approx \exp(\nu_{ion}t)$, so that the density of electrons is $n_e(t) = N_e(t)/V(t) \approx 3\exp(\nu_{ion}t)/4\pi\delta(t)^3$. While the plasma radius $\delta(t)$ is smaller than the Debye length, it is assumed to be the mean radius of a 3D random walk process, $\delta(t) = L_e\sqrt{N_c} = \sqrt{3T_e t/\nu_m m_e}$, where $L_e = \nu_m^{-1}\sqrt{3T_e/m_e}$ is the electron mean-free-path in air and $N_c = \nu_m t$ is the number of collisions. The electron momentum-loss collision rate ν_m is given in Appendix 2.B. After the plasma radius reaches the Debye length $\lambda_D = \sqrt{\varepsilon_0 T_e/n_e e^2}$, the diffusion process is assumed to be ambipolar [46], and the plasma radius effectively stops increasing. The temperature is assumed to be the steady-state temperature derived in a previous section, $T_e = T_{ss}(I_0, \lambda)$. The breakdown time τ_{se} for a single electron-seeded avalanche ionization is shown in Fig. 2.6a as a function of CW laser intensity for several values of the laser wavelength, using a breakdown density of $n_{bd} = 10^{18}$ cm^{-3}. Figure 2.6b shows the maximum plasma radius δ_{max} reached during the breakdown ionization.
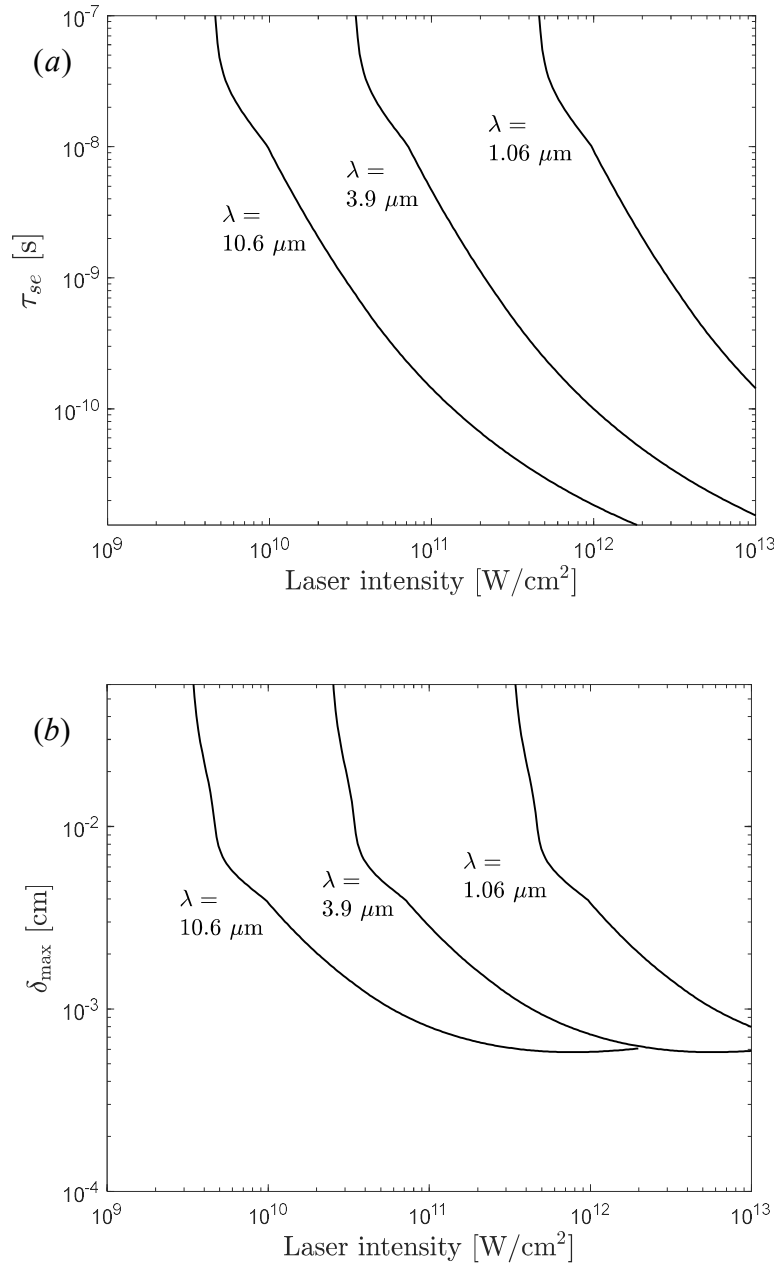
Figure 2.6. (a) CW breakdown time (time to reach $n_{bd} = 10^{18}$ cm^{-3}) and
(b) maximum plasma radius for avalanche seeded by one electron. Shown
for several values of laser wavelength as a function of laser intensity.

The example in the previous section considered a 50 ns, $\lambda = 10.6$ μm square

pulse of intensity $I_0 = 5 \times 10^9$ W/cm^2 and focused area 2.5×10^{-3} cm^2. In this case, the

single-electron breakdown time, with $n_{bd} = 10^{18}$ cm^{-3}, is 43 ns and the plasma reaches a

maximum radius of $\delta = 74$ μm before the transition to ambipolar diffusion. For initial

electron densities greater than $n_e(0) \sim 10^6$ cm^{-3}, the continuum approximation can be

employed, and the breakdown time can be used as a signature of the presence of excess

radioactivity. If, however, this pulse is used to initiate breakdown seeded by electron

densities below 10^6 cm^{-3}, including the background ion density of $\sim 10^3$ cm^{-3},

determination between regions of different ion density cannot be made based on

differential single-shot measurements of the breakdown time. In this case, a laser pulse

with different parameters should be used, or a statistical method should be employed [3],

[37].

2.3. Proof-of-concept experiments

Experiments performed at the University of Maryland have demonstrated that

photo-detachment of negative ions can seed avalanche ionization, and that this can be

used to detect radioactive materials [3]. These experiments were performed in a

parameter regime where a continuum of ions and electrons could not be assumed,

however the basic physics of the experiment is the same as that presented in this chapter.

The experiment used a Polonium-210 alpha source to irradiate air, producing an elevated

negative ion density. A $\sim$ 50 ps (FWHM), chirped, $\lambda = 3.9$ μm laser pulse, with intensity
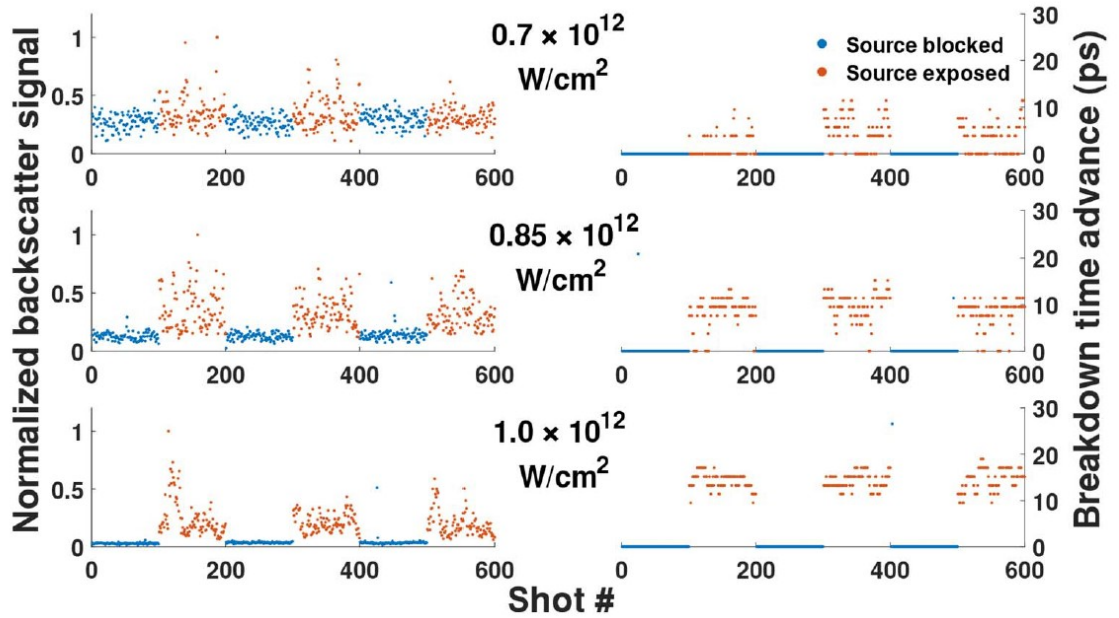
Figure 2.7. (from [3]) "On-off response of breakdowns to a modulated external source of radioactivity. A series of shots measured the pump backscatter (left) and breakdown time advance (right) as the α irradiation was periodically switched on and off using a mechanical shutter."

from 0.6 TW/cm^2 to 1.3 TW/cm^2, was used to both photo-detach negative ions and drive breakdown. Breakdown was measured by observing a chirped probe beam, $\lambda = 1.45\ \mu m$, co-propagating with the pump, as well as by measuring pump radiation back-scattered from the breakdown plasma. The chirped probe allowed measurement of the breakdown time advance, or the amount of time between the saturation of the breakdown process and the end of the pump pulse.

As the radioactive source was covered and uncovered, on-off behavior was observed in both the backscatter signal as well as in measurement of the breakdown time advance (Fig. 2.7).

2.4. Conclusion

We have presented and analyzed a concept for the remote detection of radioactivity by active observation of electromagnetic signatures. The presence of ionizing radiation results in an elevated density of negative ions. These ions may be photo-detached by an incident laser beam, producing a population of seed electrons for a subsequent laser-induced avalanche ionization air breakdown. In the appropriate laser parameter regimes, differences in the initial seed electron density can be correlated with differences in the time required for avalanche breakdown to occur, providing a signature for the presence of radioactive materials. We have analyzed a theoretical detection example, in which a 50 ns, $\lambda = 10.6\ \mu m$ square laser pulse of intensity $I_0 = 5 \times 10^9\ W/cm^2$ is used along with a $\lambda = 1\ \mu m$ photo-detaching pre-pulse to differentiate between a region of high radioactivity ($n_i = 10^8\ cm^{-3}$) and moderate radioactivity ($n_i = 10^6\ cm^{-3}$). We found that the time delay difference between the two cases is ~ 7 ns, which is readily measureable.

Experiments have demonstrated that photo-detachment of negative ions can seed avalanche ionization, and that this can be used to detect radioactive materials [3]. These experiments were performed in a regime where a continuum of ions and electrons could not be assumed, however the basic physics of the experiment is the same as that presented in this chapter.

Appendix 2.A: Air chemistry rates

In this appendix the various air chemistry rates, ionization rates and other functions used in this analysis are discussed and expressed as functions of electron temperature. It should be noted that these are approximate expressions. However, they should be able to capture the general behavior of the mechanism.

2.A.1. Electron and ion loss terms

For a weakly ionized plasma, electrons are depleted mainly through three-body attachment to O_2. Free electrons can also recombine with positive ions, a rate which becomes important at large electron densities. The electron attachment rate to neutral oxygen (in air with temperature 300 K) is [47]

$$\nu_a[\text{s}^{-1}] = n_n^2 \times \left(\begin{array}{l} 4.85 \times 10^{-32}\, T_e^{-1}\, \exp\left(2.4\ (T_e - 0.0256)/T_e\right) \\ +\ 5.55 \times 10^{-35}\, T_e^{-2}\, \exp\left(5.1\ (T_e - 0.0256)/T_e\right) \end{array} \right) \tag{2.A1}$$

where T_e is the electron temperature in eV and n_n is the neutral density in cm^{-3}. For $T_e = 1$ eV and weak ionization, $\nu_a \approx 4.8 \times 10^7$ s^{-1}.

The electron-positive ion recombination rate coefficient is [48]

$$\beta_{e+}[\text{cm}^3 \cdot \text{s}^{-1}] = \begin{cases} 1.5 \times 10^{-8} T_e^{-0.7}, & T_e \leq 0.1 \ \text{eV} \\ 2.1 \times 10^{-8} T_e^{-0.5}, & T_e > 0.1 \ \text{eV} \end{cases} \quad \text{for } e + O_2^+, \\ 4.3 \times 10^{-8} T_e^{-0.39} \qquad\qquad\qquad \text{for } e + N_2^+. \tag{2.A2}$$

This rate is important when the plasma is nearly fully ionized, however it has not been

used in our simulations, which mainly model weak ionization, $n_e \ll n_n$. Additionally, the

recombination rate is an important factor in determining the plasma decay time.

The rate coefficient for mutual neutralization of positive and negative ions is a

function only of the gas temperature, taken to be 300 K, and has the value

$\beta_\pm = 1.56 \times 10^{-7}$ cm^3 s^{-1} for $O_2^- + N_2^+$ and $\beta_\pm = 4.12 \times 10^{-7}$ cm^3 s^{-1} for $O_2^- + O_2^+$ [48].

The rate coefficient for detachment of O_2^- by collision with N_2 is likewise a

function only of the gas temperature, and is $\beta_n = 9.97 \times 10^{-20}$ cm^3 s^{-1} for 300 K air [48].

2.A.2. Collisional ionization rate

The rate of collisional ionization used in our model is [49]

$$\beta_{N_2}[\text{cm}^3\text{s}^{-1}] = T_e^{-1/2} \exp\left(-15.58/T_e\right) f_{N_2}\left(T_e\right),$$

$$f_{N_2}\left(T_e\right) = \begin{cases} -7.87 \times 10^{-10} + 6.12 \times 10^{-9} T_e \\ +1.04 \times 10^{-9} T_e^2 \end{cases}, \quad 0 \text{ eV} < T_e < 5 \text{ eV} \\ \begin{cases} -3.16 \times 10^{-8} + 1.70 \times 10^{-8} T_e \\ +9.34 \times 10^{-11} T_e^2 \end{cases}, \quad 5 \text{ eV} < T_e < 25 \text{ eV} \tag{2.A3a}$$

for ionization of N_2 and

$$\beta_{O_2}[\text{cm}^3\text{s}^{-1}] = T_e^{-1/2} \exp\left(-12.06/T_e\right) f_{O_2}\left(T_e\right),$$

$$f_{O_2}\left(T_e\right) = \begin{cases} 3.03 \times 10^{-10} + 1.46 \times 10^{-9} T_e \\ +9.27 \times 10^{-10} T_e^2 \end{cases}, \quad 0 \text{ eV} < T_e < 5 \text{ eV} \\ \begin{cases} -2.95 \times 10^{-8} + 1.08 \times 10^{-8} T_e \\ +2.45 \times 10^{-10} T_e^2 \end{cases}, \quad 5 \text{ eV} < T_e < 25 \text{ eV} \tag{2.A3b}$$

for ionization of O_2. The rate of dissociative ionization at these temperatures is much

smaller, and is not considered here. The total rate of collisional ionization in air is then

$$\nu_{coll}[\text{s}^{-1}] = \left(0.8\,\beta_{N_2} + 0.2\,\beta_{O_2}\right)n_n .$$

Appendix 2.B: Electron heating and cooling

2.B.1. Resistive (inverse Bremsstrahlung) heating

Electrons in the presence of a laser field gain energy at an average rate

$\langle \mathbf{J} \cdot \mathbf{E} \rangle = \left(\omega_p^2 / 8\pi\right) E_{eff}^2 / \nu_e$. (in cgs units), where ω_p is the plasma frequency, and the

effective electric field E_{eff} is defined as $E_{eff} = (1 + \omega^2 / \nu_m^2)^{-1/2} E_0 \approx E_0 \left(\nu_m / \omega\right)$. This is

the result of solving the electron momentum equation with a simple collision rate of

momentum transfer, ν_m, and then taking a time average [45]. Expressed in more

convenient units and variables, the rate of electron energy density increase is

$$\frac{3}{2} \frac{\partial(n_e T_e)}{\partial t}\bigg|_{heat} = \langle \mathbf{J} \cdot \mathbf{E} \rangle [\text{eV} \cdot \text{cm}^{-3}\text{s}^{-1}] \qquad (2.A4)$$
$$= 1.88 \times 10^{-13} n_e \lambda^2 I_0 \nu_m ,$$

where λ and ω are the wavelength in μm and the angular frequency of the laser field in

rad/s, respectively, and I_0 is the peak intensity in W/cm^2. The electron-neutral

momentum-transfer collision rate ν_m in weakly ionized air is given by

$$\nu_m \ [\text{s}^{-1}] = n_n \times 1.86 \times 10^{-7} \left(\exp(-0.02\,T_e) - \exp(-0.64\,T_e)\right), \qquad (2.A5)$$
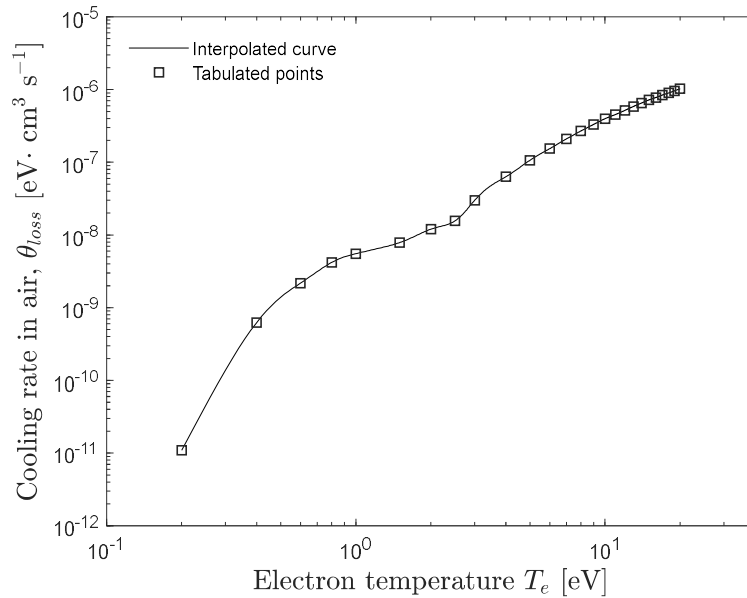
Figure 2.A1. Cooling rate coefficient as a function of electron temperature. Solid curve is interpolated from tabulated data.

which is a function fitted to tabulated data [50], calculated for electron temperatures from 0.1 eV to 30 eV.

2.B.2. Inelastic cooling of electrons

The plasma electrons lose energy through several inelastic processes, including impact excitation of vibrational and rotational modes in air molecules, collisional dissociation and ionization, as well as attachment and recombination. Energy is also lost through elastic scattering with air molecules. The exact energy-dependent cross-sections for momentum transfer, recombination and attachment are not well-known, so the energy loss rates have been approximated by multiplying the rate of each process by the average

energy of an electron, $3T_e / 2$. The total rate of electron energy loss can then be

expressed as

$$\varepsilon_{loss}[\text{eV} \cdot \text{s}^{-1}] = \frac{1}{n_e} \frac{3}{2} \frac{\partial(n_e T_e)}{\partial t}\bigg|_{loss} = \frac{3}{2} T_e \left(\frac{2m}{M} \nu_m + \beta_{e+} n_+ + \nu_a \right) + n_n \theta_{loss}, \qquad (2.\text{A7})$$

where θ_{loss} is the total rate coefficient for cooling due to rotational and vibrational

excitation, ionization, and dissociation. Values for θ_{loss} were interpolated from tabulated

data [51], and have been plotted in Fig. 2.A1. For weak ionization and $T_e > 0.2$ eV, the

term $n_n \theta_{loss}$ is much larger than all other cooling terms.

Chapter 3. Proton acceleration in a slow wakefield

3.1. Introduction

Laser wakefield acceleration of electrons has proven to be a promising avenue of investigation for the production of high-energy electrons over short distances [15], [52], [53], with maximum energies up to several GeV having been demonstrated experimentally [54]. A single-pulse laser wakefield in a plasma has a phase velocity of ~ c, and is not suitable for the acceleration of ions, because the initial ion velocity is much less than c and must increase by several orders of magnitude.

Current mechanisms for acceleration of ions, in particular protons, require either large acceleration distances of multiple meters in the case of conventional RF linacs or synchrotrons [55], or multi-TW to PW laser systems [56], [57]. Some proposed alternatives include vacuum acceleration in a laser beat wave [58] (a method also proposed for acceleration of electrons [15][59]) or in a plasma wave produced by backward Raman scattering [60]. However, these require laser pulse characteristics which are currently challenging.
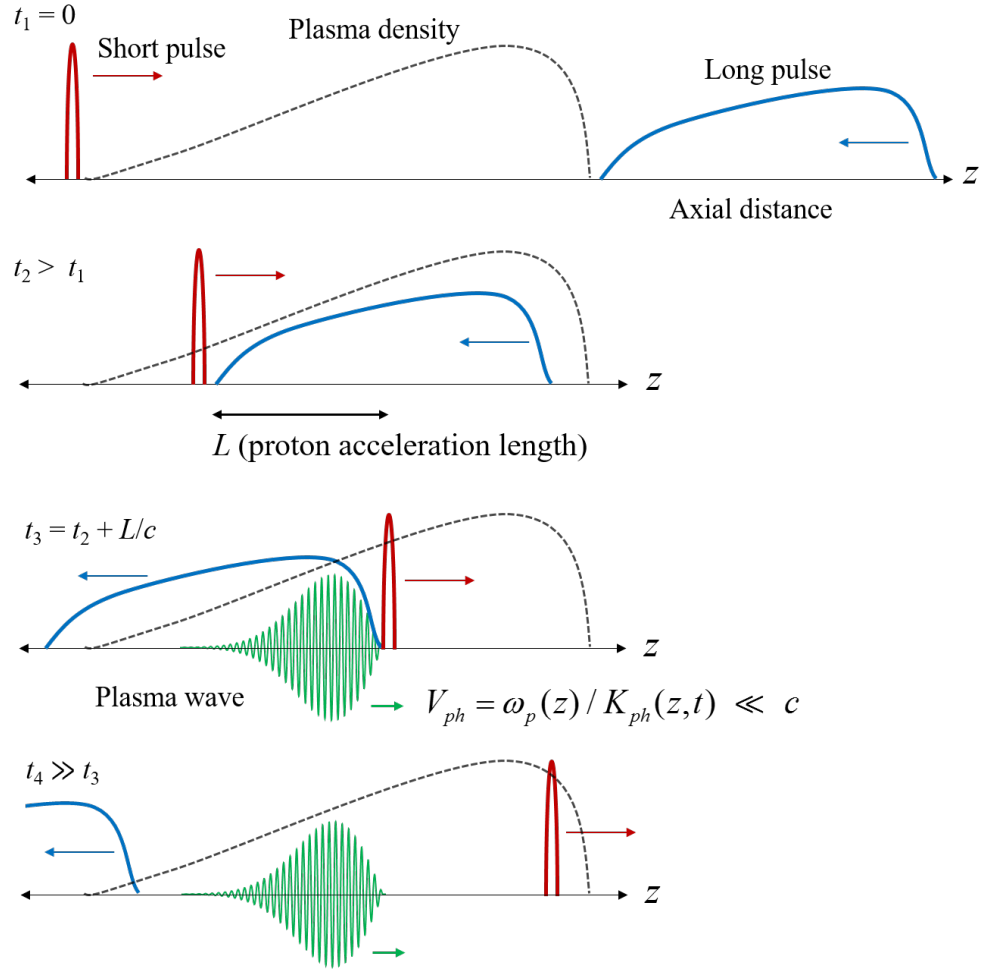
Figure 3.1. Two counter-propagating laser pulses, one short and one long, interact in a region with a spatially varying plasma density (dotted line). A slow wakefield (green) is shock-excited in the interaction region, with an initial wave-number equal to the sum of those of the two laser pulses. The frequency of the wakefield is the plasma frequency and the group velocity (envelope) is zero. (not to scale)

We propose a mechanism for proton acceleration from close to rest up to and beyond ~ 10 MeV ($\sim 0.15\ c$) in a slow wakefield (Fig. 3.1). The slow wakefield is shock-excited by the beat wave generated in a plasma by two counter-propagating laser pulses.

The phase velocity and amplitude of the wakefield can be appropriately controlled to permit proton trapping and acceleration. The slow wakefield has been analyzed theoretically, and modeled numerically. We present and discuss an example of proton acceleration to 10 MeV in a distance of ~ 1 cm. In addition, a fluid simulation is performed (turboWAVE) showing the excitation of the slow wakefield which would allow acceleration up to 1 MeV (proof of concept). Full simulation of the acceleration process was deemed to be computationally unfeasible at this time.

3.2. Acceleration model

3.2.1. Slow wakefield

It can be shown that the equation for the wakefield's electric field E_{PW} in a variable-density plasma with frequency $\omega_p(z)$ driven by a ponderomotive force is [61]

$$\frac{\partial^2 E_{PW}}{\partial t^2} + \omega_p^2(z) E_{PW} = -\frac{m c^2}{|q|} \frac{\omega_p^2(z)}{2} \frac{\partial (\mathbf{a} \cdot \mathbf{a}(z,t))}{\partial z} \ , \tag{3.1}$$

where m and q are the electron mass and charge. The effects of electron collisions have not been included in Eq. 3.1, but will be discussed later. The total normalized vector potential of the laser field is $\mathbf{a} = q\mathbf{A}/m_e c^2 = \mathbf{a}_0 + \mathbf{a}_1$, $\mathbf{E} = -\partial \mathbf{A}/c\partial t$, where the forward-propagating laser pulse is

$$\mathbf{a}_0 = \hat{a}_0(t - z/c)\sin(k_0 z - \omega_0 t + \theta_0) \ , \tag{3.2a}$$

and the backward-propagating laser pulse is

$$\mathbf{a}_1 = \hat{a}_1(t+z/c)\cos\left(k_1 z + \omega_1 t + \theta_1\right) . \tag{3.2b}$$

The wavenumbers of the pulses are k_0 and k_1, the frequencies are ω_0 and ω_1, and θ_0 and θ_1 are the initial phases at $z=0$. The pulse amplitude envelopes are $\hat{a}_0$ and $\hat{a}_1$. Written as a function of the laser pulse parameters, the normalized vector potential is

$a = 8.6\times10^{-10}\lambda[\mu m]I^{1/2}[\text{W/cm}^2]$.

The cross term in the product $\mathbf{a}\cdot\mathbf{a}$ in Eq. 3.1 contains the slow-phase-velocity beat wave and excites the slow wakefield, i.e.,

$\mathbf{a}\cdot\mathbf{a} = 2\mathbf{a}_0\cdot\mathbf{a}_1 + \ldots = \hat{a}_0(t-z/c)\hat{a}_1(t+z/c)\sin\Psi(z,t) + \ldots$, where the phase of the beat wave is

$$\Psi(z,t) = K z - \Delta\omega_{01} t + \theta_{01}, \tag{3.3}$$

where $K = k_0 + k_1$, $\Delta\omega_{01} = \omega_0 - \omega_1$, and $\theta_{01} = \theta_0 + \theta_1$. The forward going pulse, $|\mathbf{a}_0| < 1$, is short compared to a plasma period, hence the amplitude of the excited fast wakefield is small.

The forward-propagating short pulse with duration $\Delta\tau$ can be represented by $\hat{a}_0 = a_0 \Delta\tau \delta(t-z/c)$. Equation 3.1 has the forward-propagating solution

$E_{WF}(z,t) = (\omega_p(z)/\omega_0)\hat{E}_0(z)\sin\Phi(z,t)$, where

$$\hat{E}_0(z) = \frac{1}{4}\frac{mc^2}{|q|}a_0\hat{a}_1(2z/c)\Delta\tau\,\omega_0\left(K - \Delta\omega_{01}/c + \omega_p(z)/c\right),\qquad (3.4a)$$

and

$$\Phi(z,t) = \Psi(z,z/c) - \omega_p(z)(t - z/c).\qquad (3.4b)$$

The delta-function representation for $\hat{a}_0$ is valid as long as $\left|\omega_p(z) - \Delta\omega_{01}\right|\Delta\tau \ll 1$.

The phase velocity of the slow wakefield is

$$V_{phase}(z,t) = -\frac{\partial\Phi/\partial t}{\partial\Phi/\partial z} = \frac{\omega_p(z)}{K_p(z,t)} \ll c,\qquad (3.5)$$

where $K_p(z,t) = K - \Delta\omega_{01}/c + \omega_p(z)/c - \left(\partial\omega_p/\partial z\right)(t - z/c)$ and $K - \Delta\omega_{01}/c = 2k_1$. The

phase velocity depends only on the characteristics of the backward-propagating laser

pulse and the plasma density gradient. In a positive density gradient, the phase velocity

increases as a function of time.

3.2.2. Proton acceleration

The equation of motion for a proton at position $z(t)$ is

$$\frac{dV_z(t)}{dt} = \frac{|q|}{M}E_{WF}(z(t),t) - \frac{c^2}{2}\left(\frac{m}{M}\right)^2\left(\frac{\partial\mathbf{a}\cdot\mathbf{a}(z(t),t)}{\partial z}\right),\qquad (3.6)$$

where the first term on the right-hand side is the force due to the wakefield, the second term is the vacuum ponderomotive force of the laser fields, and M is the proton mass. The vacuum term provides no net gain of energy in the absence of the short pulse.

The phase $\Phi(z(t),t)$ (Eq. 3.4b) of a resonant proton will oscillate about a resonant phase Φ_R. If the wave's phase velocity is changing, the acceleration dV_z / dt of the proton must be equal to the acceleration of the wave, evaluated at the position of the proton: $dV_z / dt = dV_{ph} / dt = \partial V_{ph} / \partial t + V_z \partial V_{ph} / \partial z$. The resonant phase is given by

$$\sin \Phi_R \approx \frac{2}{K_p^2(z(t),t)} \frac{\partial \omega_p(z(t))}{\partial z} \frac{M}{|q|} \frac{\omega_0}{\hat{E}_0(z(t))} \ . \tag{3.7}$$

Since $\left|\sin \Phi_R\right| \leq 1$, Eq. 3.7 places requirements on the plasma density gradient and wakefield amplitude.

When the proton is close to resonance, its phase can be expressed as a small deviation about the resonant phase, $\Phi(t) = \Phi_R + \delta\Phi(t)$. The pendulum-like equation for this phase deviation is

$$\frac{d^2 \delta\Phi}{dt^2} + \Omega_1(z(t),t)\frac{d\delta\Phi}{dt} + \Omega_0^2(z(t),t)\delta\Phi = 0 \ , \tag{3.8}$$

where $\Omega_0^2(z,t) = -K_p(z,t)\frac{|q|}{M}\frac{\omega_p(z)}{\omega_0}\hat{E}_0(z)\cos\Phi_R$ and $\Omega_1(z,t) = \frac{2}{K_p(z,t)}\frac{\partial \omega_p(z)}{\partial z}$. For the proton to remain trapped (resonant) and accelerated, the amplitude of the oscillations $\delta\Phi(t)$ should remain small. From Eq. 3.8, this implies $\Omega_0^2(z(t),t) > \Omega_1^2(z(t),t)/4$,

66

$\hat{E}_0 < 0$, $\sin \Phi_R < 0$ and $\cos \Phi_R > 0$, assuming the parameters (frequencies) Ω_0 and Ω_1 vary slowly in time.

3.2.3. Wave breaking and acceleration conditions

The stability conditions implied by Eq. 3.8 introduce a lower bound on the amplitude of the wakefield. A conservative upper bound is the wave-breaking field [62],

$$E_{WB}(z,t) = \left(\frac{m_e c^2}{q} (\omega_p(z)/c) \right) \frac{V_{ph}}{c} \, , \tag{3.9}$$

which is the wave-breaking field of a fast, single-pulse laser wakefield [52] reduced by the factor V_{ph}/c. This upper bound in the wakefield amplitude translates into a limit on the acceleration of the proton, and therefore places a constraint on the plasma density profile. The limit is represented by the inequality $\Omega_1(z(t),t)/\omega_p(z(t)) \lesssim m_e/M$.

3.2.4. Collision damping and Raman instabilities

The electron-ion collision frequency is v_{ei} [s^{-1}] $\approx 10^{-5} n_0 [\mathrm{cm}^{-3}]/T_e^{3/2}[\mathrm{eV}]$, where T_e is the effective temperature of the electrons [63]. For electrons in a laser field with normalized amplitude a, the effective electron temperature is due to the electron quiver velocity. The effective temperature is T_e [eV] $\sim a^2 m_e c^2$, and the characteristic collision time, which can be treated as a characteristic time for the damping of the wakefield, is τ_{ei} [s] $= 1/v_{ei} \approx 3.64 \times 10^{13} a^3/n_0$ [cm^{-3}] . If collisions are included in Eq. 3.1, a term

$-4\pi |q| n_0 \nu_{ei} \delta \upsilon_z$ appears on the right-hand-side, where $\delta \upsilon_z$ is the axial electron fluid velocity. This term can be neglected if $\nu_{ei} \ll \omega_p(z)$, a condition that is satisfied in our example. In the absence of an external laser field, once the long backward-going pulse has propagated out of the interaction region, the wakefield will be damped. In this case, it may be necessary to include a third laser pulse to extend the damping time.

Instabilities such as the Raman instability can be driven in the acceleration region. This can amplify the forward-propagating short pulse (Backward-Raman-Amplification [64]). The three-wave instability can also grow from noise via the interaction of the long backward-propagating pulse with the plasma. The growth rate and the condition for suppression for both of these is the same. The stimulated Raman scattering instability will be suppressed in an inhomogeneous plasma if the e-folding length of the instability is longer than the characteristic gradient of the plasma density. The approximate condition for suppression of the instability is [65]

$$\Gamma_0 < \left(\frac{\omega_p(z)}{K_p(z,t)} \left| \frac{\partial \omega_p(z)}{\partial z} \right| \right)^{1/2} , \tag{3.10}$$

where the growth rate is $\Gamma_0 = \hat{a}_1(t + z/c) \left(\omega_p(z) \, \omega_1 / 4 \right)^{1/2}$ [66]. In the examples presented in the next section, this condition is easily satisfied in regions where the wakefield has already been excited. It is, however, only marginally satisfied elsewhere. It may be necessary to include a chirp on the long pulse to further suppress growth of the instability from noise, and/or to modify the ratio of pulse amplitudes. Similarly,
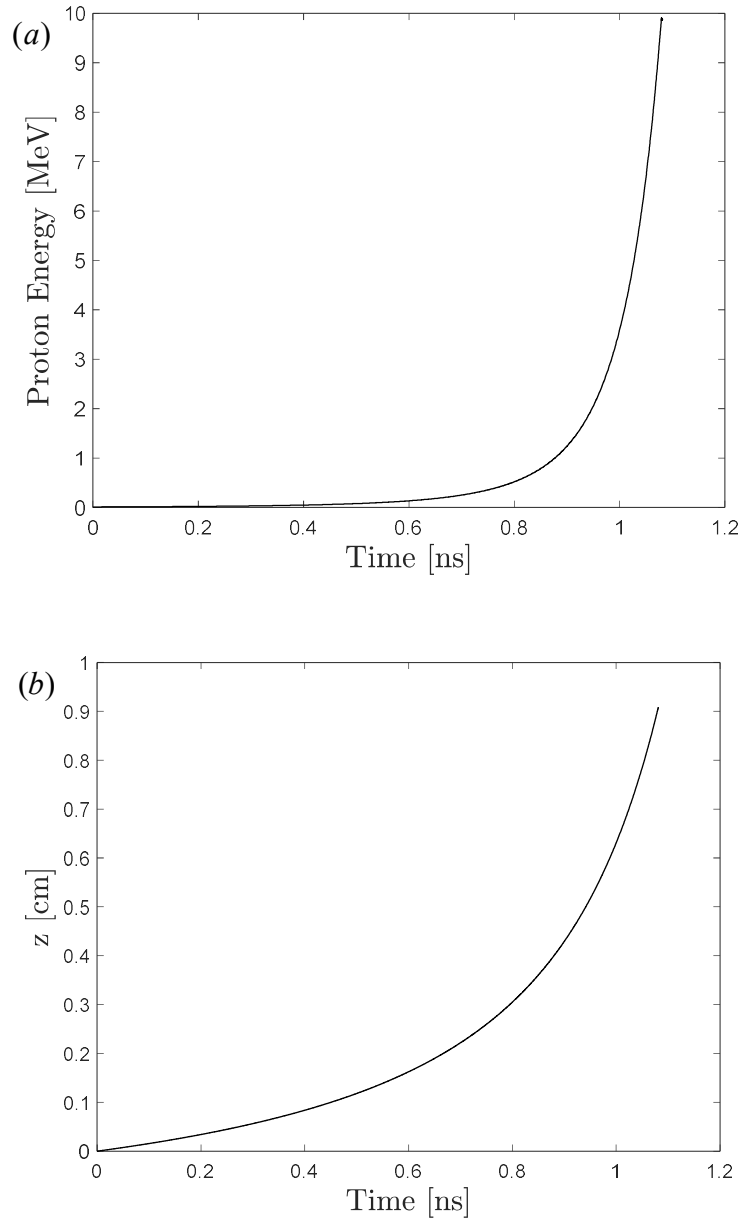
Figure 3.2. (a) Energy and (b) displacement of an accelerated proton in the analytically derived wakefield. The short pulse has wavelength 800 nm and the long pulse is 828 nm. The long pulse has a duration of ~ 80 ps, with peak normalized amplitude product $a_0 a_1 = 1.3 \times 10^{-3}$.

amplification of the short pulse was observed in simulation in the region where the frequency-matching condition was approximately satisfied, but may be suppressed or amplified depending on the chirp on the backward-propagating pulse. The chirp may also provide an additional control on the phase velocity of the slow wakefield.

3.3. Simulation results

3.3.1. 10 MeV acceleration example

To illustrate the acceleration mechanism, a proton test charge can be placed in the analytically derived forward-going slow wakefield. Figures 3.2a and 3.2b show the proton energy and distance for an accelerated test charge with an initial energy of 10 keV. This energy would require injection of protons rather than trapping from resonant background protons. Injection might be accomplished by direct ponderomotive acceleration by a laser beat wave, for example[15], [58], [59].

The laser parameters for this example correspond to a 5 GW long pulse (828 nm for ~ 80 ps) and 1 TW short pulse (800 nm for 20 fs). Both beams are assumed to have a 50 μm spot size, with a Rayleigh length longer than the acceleration distance. For these parameters, the long pulse energy is ~ 400 mJ and the short pulse is ~ 30 mJ. The laser and plasma density profiles in this example were chosen so that the accelerating field does not significantly exceed wavebreaking, but has an amplitude sufficient to trap protons. The plasma density was chosen to increase quadratically from ~ 10^{17} cm^{-3} to ~ 5 x 10^{18} cm^{-3} over a distance of ~ 1 cm. Trapping and acceleration of resonant protons occurs over many hundreds of wavelengths of the slow wakefield, and in a large fraction
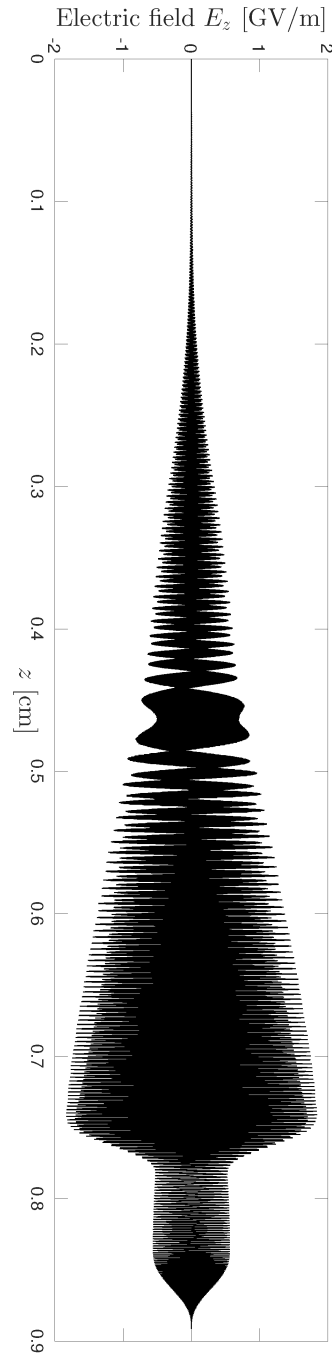
Figure 3.3. Accelerating electric field of a slow wakefield. The short $\lambda = 800$ nm pulse has $a_0 = 0.12$ and $\Delta\tau = 20$ fs. The long $\lambda = 828$ nm pulse has $a_1 = 0.004$ and duration ~ 50 ps. Grid spacing is $\Delta z = 8.5$ nm and timestep is $\Delta t = 14$ as. Plasma density is negligible at $z = 0$ and increases to $n_0 = 4 \times 10^{18}$ cm^{-3} at $z = 0.75$ cm.

of each wavelength. The final energy of the protons depends on the particular wavelength in which they are trapped.

3.3.2. Proof-of-concept simulation of accelerating wakefield

A full-scale PIC simulation of the acceleration of protons to ~ MeV energies in a slow wakefield was deemed computationally unfeasible. As a preliminary proof-of-concept, simulation in a fluid model of the excitation of a slow wakefield in a density gradient has been performed, with parameters shown by analysis to be suitable for proton acceleration from 50 keV at $z = 0.33$ cm to ~ 1 MeV at $z = 0.75$ cm. The electric field of the wakefield is shown in Fig. 3.3. PIC protons were not placed in the wakefield, as acceleration would take much longer than excitation of the accelerating field.

3.4. Discussion

A mechanism for the acceleration of protons in a laser wakefield has been proposed, which could allow energies up to 10 MeV in a short distance ~ 1 cm. The analysis presented here is performed in a one-dimensional limit. This mechanism has the potential to produce high-quality quasi-monoenergetic proton bunches of low emittance. This is because in the linear regime protons can undergo transverse focusing [52]. The controlled production of high-density gas jets has also been demonstrated experimentally [67]. One potential application for protons at this energy is the generation of short-lived radioisotopes for use in Positron Emission Tomography (PET). Current production of these radio-pharmaceuticals is limited and expensive. The approximate requirement for

this is an average flux 10^{12} protons/sec, with energy greater than 5 MeV [68][69]. For the example given in this chapter of acceleration up to 10 MeV, an estimation assuming a 50 μm laser spot size gives a required repetition rate in the kHz range.

There are several issues and challenges which might impact the proposed mechanism. One of these is the collisional damping of the slow wakefield. Damping can be mitigated by the introduction of a long third laser pulse such that the characteristic collision time is on the ns time scale. For a plasma density $\lesssim 5 \times 10^{18}$ cm^{-3}, this requires a normalized pulse amplitude $a > 0.05$, equivalent to, for example, a 1 J pulse of a TEA CO_2 laser.

Another issue to consider is the possible presence of Raman instabilities in the laser plasma. One such instability can be excited by the long backward-going pulse. Raman instabilities can also amplify the forward-going pulse, via Backward Raman Amplification. This will increase the amplitude of the wakefield, which could result in loss of trapping and/or extreme wavebreaking. While this effect is difficult to analyze, it can be corrected for in experiments by the appropriate choice of pulse amplitude profile on the backward-going wave. The increase in pulse amplitude may also prove useful for exciting the slow wakefield with a lower-intensity pulse than might otherwise be required.

Bibliography

[1]   J. Isaacs and P. Sprangle, "Effect of laser noise on the propagation of laser radiation in dispersive and nonlinear media," *J. Opt. Soc. Am. B*, vol. 36, no. 2, pp. 346–355, Feb. 2019.

[2]   J. Isaacs, C. Miao, and P. Sprangle, "Remote monostatic detection of radioactive material by laser-induced breakdown," *Physics of Plasmas*, vol. 23, no. 3, p. 033507, 2016.

[3]   R. M. Schwartz, D. Woodbury, J. Isaacs, P. Sprangle, and H. M. Milchberg, "Remote detection of radioactive material using mid-IR laser–driven electron avalanche," *Science Advances*, vol. 5, no. 3, 2019.

[4]   J. Isaacs and P. Sprangle, "Proton acceleration in a slow wakefield," *Applied Physics Letters*, vol. 110, no. 2, p. 024101, 2017.

[5]   P. Sprangle and B. Hafizi, "High-power, high-intensity laser propagation and interactions," *Physics of Plasmas*, vol. 21, no. 5, p. 055402, 2014.

[6]   P. Sprangle, B. Hafizi, H. Milchberg, G. Nusinovich, and A. Zigler, "Active remote detection of radioactivity based on electromagnetic signatures," *Physics of Plasmas*, vol. 21, no. 1, p. 013103, 2014.

[7]   Z. Epstein and P. Sprangle, "An Optical Magnetometry Mechanism Above the Surface of Seawater," *IEEE Journal of Quantum Electronics*, vol. 52, no. 6, pp. 1–6, Jun. 2016.

[8]   P. Sprangle, J. Peñano, B. Hafizi, D. Gordon, and M. Scully, "Remotely induced atmospheric lasing," *Applied Physics Letters*, vol. 98, no. 21, p. 211102, 2011.

[9]   J. R. Peñano, P. Sprangle, P. Serafim, B. Hafizi, and A. Ting, "Stimulated Raman scattering of intense laser pulses in air," *Phys. Rev. E*, vol. 68, no. 5, p. 056502, Nov. 2003.

[10] P. Sprangle, B. Hafizi, A. Ting, and R. Fischer, "High-power lasers for directed-energy applications," *Appl. Opt.*, vol. 54, no. 31, pp. F201–F209, Nov. 2015.

[11] P. Sprangle, J. R. Peñano, and B. Hafizi, "Propagation of intense short laser pulses in the atmosphere," *Phys. Rev. E*, vol. 66, no. 4, p. 046418, Oct. 2002.

[12] M. Lampe, R. F. Fernsler, S. P. Slinker, and D. F. Gordon, "Traveling wave model for laser-guided discharges," *Physics of Plasmas*, vol. 17, no. 11, p. 113511, 2010.

[13]   D. F. Gordon, A. Ting, R. F. Hubbard, E. Briscoe, C. Manka, S. P. Slinker, A. P. Baronavski, H. D. Ladouceur, P. W. Grounds, and P. G. Girardi, "Streamerless guided electric discharges triggered by femtosecond laser filaments," *Physics of Plasmas*, vol. 10, no. 11, pp. 4530–4538, 2003.

[14]   A. Morozov, Y. Luo, S. Suckewer, D. F. Gordon, and P. Sprangle, "Propagation of ultrashort laser pulses in optically ionized gases," *Physics of Plasmas*, vol. 17, no. 2, p. 023101, 2010.

[15]   E. Esarey, P. Sprangle, J. Krall, and A. Ting, "Overview of plasma-based accelerator concepts," *IEEE Transactions on Plasma Science*, vol. 24, no. 2, pp. 252–288, Apr. 1996.

[16]   P. Sprangle, E. Esarey, A. Ting, and G. Joyce, "Laser wakefield acceleration and relativistic optical guiding," *Applied Physics Letters*, vol. 53, no. 22, pp. 2146–2148, 1988.

[17]   G. Agrawal, *Nonlinear Fiber Optics (Fifth Edition)*. Boston: Academic Press, 2013.

[18]   R. W. Boyd, *Nonlinear Optics (Third Edition)*, Third Edition. Burlington: Academic Press, 2008.

[19]   M. Erkintalo, G. Genty, B. Wetzel, and J. M. Dudley, "Limitations of the linear Raman gain approximation in modeling broadband nonlinear propagation in optical fibers," *Opt. Express*, vol. 18, no. 24, pp. 25449–25460, Nov. 2010.

[20]   S. Zahedpour, J. K. Wahlstrand, and H. M. Milchberg, "Measurement of the nonlinear refractive index of air constituents at mid-infrared wavelengths," *Opt. Lett.*, vol. 40, no. 24, pp. 5794–5797, Dec. 2015.

[21]   Y. S. Kivshar and G. Agrawal, *Optical Solitons: From Fibers to Photonic Crystals*. Elsevier Science, 2003.

[22]   G. Fibich and A. L. Gaeta, "Critical power for self-focusing in bulk media and in hollow waveguides," *Opt. Lett.*, vol. 25, no. 5, pp. 335–337, Mar. 2000.

[23]   J. J. Pigeon, S. Y. Tochitsky, C. Gong, and C. Joshi, "Supercontinuum generation from 2 to 20 μm in GaAs pumped by picosecond CO2 laser pulses," *Opt. Lett.*, vol. 39, no. 11, pp. 3246–3249, Jun. 2014.

[24]   G. D. Domenico, S. Schilt, and P. Thomann, "Simple approach to the relation between laser frequency noise and laser line shape," *Appl. Opt.*, vol. 49, no. 25, pp. 4801–4807, Sep. 2010.

[25] W. K. Marshall, B. Crosignani, and A. Yariv, "Laser phase noise to intensity noise conversion by lowest-order group-velocity dispersion in optical fiber: exact theory," *Opt. Lett.*, vol. 25, no. 3, pp. 165–167, Feb. 2000.

[26] J. Wang and K. Petermann, "Small signal analysis for dispersive optical fiber communication systems," *Journal of Lightwave Technology*, vol. 10, no. 1, pp. 96–100, Jan. 1992.

[27] W. K. Marshall and A. Yariv, "Spectrum of the intensity of modulated noisy light after propagation in dispersive fiber," *IEEE Photonics Technology Letters*, vol. 12, no. 3, pp. 302–304, Mar. 2000.

[28] D. Engin, W. Lu, M. Akbulut, B. McIntosh, H. Verdun, and S. Gupta, "1 kW cw Yb-fiber-amplifier with <0.5GHz linewidth and near-diffraction limited beam-quality for coherent combining application," *Proc.SPIE*, vol. 7914. pp. 7914 – 7914 – 7, 2011.

[29] V. Gapontsev, D. Gapontsev, N. Platonov, O. Shkurikhin, V. Fomin, A. Mashkin, M. Abramov, and S. Ferin, "2 kW CW ytterbium fiber laser with record diffraction-limited brightness," in *CLEO/Europe. 2005 Conference on Lasers and Electro-Optics Europe, 2005.*, 2005, p. 508–.

[30] J. W. Goodman, *Statistical Optics*. Wiley, 2015.

[31] D. Haberberger, S. Tochitsky, and C. Joshi, "Fifteen terawatt picosecond CO2 laser system," *Opt. Express*, vol. 18, no. 17, pp. 17865–17875, Aug. 2010.

[32] S. Tochitsky, "Nonlinear guiding of picosecond CO_2 laser pulses in atmosphere(Conference Presentation)," *Proc.SPIE*, vol. 10193. pp. 10193 – 10193 – 1, 2017.

[33] A. A. Voronin and A. M. Zheltikov, "Long-wavelength infrared solitons in air," *Opt. Lett.*, vol. 42, no. 18, pp. 3614–3617, Sep. 2017.

[34] D. R. Lide, *CRC Handbook of Chemistry and Physics, 84th Edition*. Taylor & Francis, 2003.

[35] Y. S. Dimant, G. S. Nusinovich, P. Sprangle, J. Penano, C. A. Romero-Talamas, and V. L. Granatstein, "Propagation of gamma rays and production of free electrons in air," *Journal of Applied Physics*, vol. 112, no. 8, p. 083303, 2012.

[36] W. A. Hoppel, R. V. Anderson, and J. C. Willett, "Atmospheric Electricity in the Planetary Boundary Layer," in *The Earth's Electrical Environment*, The National Academies Press, 1986, p. 149.

[37] V. L. Granatstein and G. S. Nusinovich, "Detecting excess ionizing radiation by electromagnetic breakdown of air," *Journal of Applied Physics*, vol. 108, no. 6, 2010.

[38] G. S. Nusinovich, P. Sprangle, C. A. Romero-Talamas, and V. L. Granatstein, "Range, resolution and power of THz systems for remote detection of concealed radioactive materials," *Journal of Applied Physics*, vol. 109, no. 8, 2011.

[39] P. Sprangle, B. Hafizi, H. Milchberg, G. Nusinovich, and A. Zigler, "Active remote detection of radioactivity based on electromagnetic signatures," *Physics of Plasmas*, vol. 21, no. 1, p. 013103, 2014.

[40] P. Sprangle, B. Hafizi, G. Nusinovich, and A. Zigler, "Active remote detection of radioactivity base on electromagnetic signatures," U.S. Patent US9835761B22015.

[41] K. M. Ervin, I. Anusiewicz, P. Skurski, J. Simons, and W. C. Lineberger, "The Only Stable State of O2- Is the X 2π g Ground State and It (Still!) Has an Adiabatic Electron Detachment Energy of 0.45 eV," *The Journal of Physical Chemistry A*, vol. 107, no. 41, pp. 8521–8529, 2003.

[42] D. S. Burch, S. J. Smith, and L. M. Branscomb, "Photodetachment of O_2^-," *Phys. Rev.*, vol. 112, no. 1, pp. 171–175, Oct. 1958.

[43] N. M. Kroll and K. M. Watson, "Multiphoton detachment of negative ions," Stanford Research Intitute, Menlo Park CA, AD0779887, 1974.

[44] A. M. Howatson, *An Introduction to Gas Discharges: Pergamon International Library of Science, Technology, Engineering and Social Studies*. Elsevier Science, 2013.

[45] A. W. Ali, "On Laser Air Breakdown, Threshold Power and Laser Generated Channel Length," *NRL Memorandum Report*, vol. 5187, 1983.

[46] J. D. Huba, *NRL PLASMA FORMULARY Supported by The Office of Naval Research*. Washington, DC: Naval Research Laboratory, 2013, pp. 1–71.

[47] I. A. Kossyi, A. Y. Kostinsky, A. A. Matveyev, and V. P. Silakov, "Kinetic scheme of the non-equilibrium discharge in nitrogen-oxygen mixtures," *Plasma Sources Science and Technology*, vol. 1, no. 3, pp. 207–220, Aug. 1992.

[48] R. F. Fernsler and A. W. Ali, "The NRL CHMAIR Code: A Disturbed Sea Level Air Chemistry Code," *NRL Memorandum Report*, vol. 4100, 1979.

[49] S. Slinker and A. W. Ali, "Electron Excitation and Ionization Rate Coefficients For N2, O2, NO, N and O," *NRL Memorandum Report*, vol. 4756, 1982.

[50] S. Slinker and A. W. Ali, "Electron Momentum Transfer Collision Frequency in N2, O2 and Air," *NRL Memorandum Report*, vol. 5614, 1985.

[51] A. W. Ali, "Electron Energy Loss Rates in Air," *NRL Memorandum Report*, vol. 5400, 1984.

[52] P. Sprangle, E. Esarey, A. Ting, and G. Joyce, "Laser wakefield acceleration and relativistic optical guiding," *Applied Physics Letters*, vol. 53, no. 22, pp. 2146–2148, 1988.

[53] A. Ting, C. I. Moore, K. Krushelnick, C. Manka, E. Esarey, P. Sprangle, R. Hubbard, H. R. Burris, R. Fischer, and M. Baine, "Plasma wakefield generation and electron acceleration in a self-modulated laser wakefield accelerator experiment," *Physics of Plasmas*, vol. 4, no. 5, pp. 1889–1899, 1997.

[54] W. P. Leemans, A. J. Gonsalves, H.-S. Mao, K. Nakamura, C. Benedetti, C. B. Schroeder, C. Tóth, J. Daniels, D. E. Mittelberger, S. S. Bulanov, J.-L. Vay, C. G. R. Geddes, and E. Esarey, "Multi-GeV Electron Beams from Capillary-Discharge-Guided Subpetawatt Laser Pulses in the Self-Trapping Regime," *Phys. Rev. Lett.*, vol. 113, no. 24, p. 245002, Dec. 2014.

[55] M. Muramatsu and A. Kitagawa, "A review of ion sources for medical accelerators (invited)," *Review of Scientific Instruments*, vol. 83, no. 2, 2012.

[56] M. Borghesi, "Laser-driven ion acceleration: State of the art and emerging mechanisms," *Nuclear Instruments and Methods in Physics Research Section A: Accelerators, Spectrometers, Detectors and Associated Equipment*, vol. 740, pp. 6–9, 2014.

[57] M. Zepf, E. L. Clark, F. N. Beg, R. J. Clarke, A. E. Dangor, A. Gopal, K. Krushelnick, P. A. Norreys, M. Tatarakis, U. Wagner, and M. S. Wei, "Proton Acceleration from High-Intensity Laser Interactions with Thin Foil Targets," *Phys. Rev. Lett.*, vol. 90, no. 6, p. 064801, Feb. 2003.

[58] F. Peano, J. Vieira, R. A. Fonseca, R. Mulas, G. Coppa, and L. O. Silva, "Direct Acceleration of Ions With Variable-Frequency Lasers," *IEEE Transactions on Plasma Science*, vol. 36, no. 4, pp. 1857–1865, Aug. 2008.

[59] E. Esarey, R. F. Hubbard, W. P. Leemans, A. Ting, and P. Sprangle, "Electron Injection into Plasma Wakefields by Colliding Laser Pulses," *Phys. Rev. Lett.*, vol. 79, no. 14, pp. 2682–2685, Oct. 1997.

[60] S. Masuda, T. Katsouleas, and A. Ogata, "Proton acceleration in plasma waves produced by backward Raman scattering," *Nuclear Instruments and Methods in*

Physics Research Section A: Accelerators, Spectrometers, Detectors and Associated Equipment, vol. 455, no. 1, pp. 172–175, 2000.

[61] P. Sprangle, B. Hafizi, J. R. Peñano, R. F. Hubbard, A. Ting, C. I. Moore, D. F. Gordon, A. Zigler, D. Kaganovich, and T. M. Antonsen, "Wakefield generation and GeV acceleration in tapered plasma channels," *Phys. Rev. E*, vol. 63, no. 5, p. 056405, Apr. 2001.

[62] W. B. Mori and T. Katsouleas, "Wavebreaking of longitudinal plasma oscillations," *Physica Scripta*, vol. 1990, no. T30, p. 127, 1990.

[63] R. W. Schunk and A. F. Nagy, *Ionospheres*. Cambridge University Press, 2000.

[64] C.-H. Pai, M.-W. Lin, L.-C. Ha, S.-T. Huang, Y.-C. Tsou, H.-H. Chu, J.-Y. Lin, J. Wang, and S.-Y. Chen, "Backward Raman Amplification in a Plasma Waveguide," *Phys. Rev. Lett.*, vol. 101, no. 6, p. 065005, Aug. 2008.

[65] M. N. Rosenbluth, "Parametric Instabilities in Inhomogeneous Media," *Phys. Rev. Lett.*, vol. 29, no. 9, pp. 565–567, Aug. 1972.

[66] W. L. Kruer, *The physics of laser plasma interactions*. Reading, MA (US); Addison-Wesley Publishing Co., 1988.

[67] D. Kaganovich, D. F. Gordon, M. H. Helle, and A. Ting, "Shaping gas jet plasma density profile by laser generated shock waves," *Journal of Applied Physics*, vol. 116, no. 1, p. 013304, 2014.

[68] K. W. D. Ledingham, P. McKenna, T. McCanny, S. Shimizu, J. M. Yang, L. Robson, J. Zweit, J. M. Gillies, J. Bailey, G. N. Chimon, R. J. Clarke, D. Neely, P. A. Norreys, J. L. Collier, R. P. Singhal, M. S. Wei, S. P. D. Mangles, P. Nilson, K. Krushelnick, and M. Zepf, "High power laser production of short-lived isotopes for positron emission tomography," *Journal of Physics D: Applied Physics*, vol. 37, no. 16, p. 2341, 2004.

[69]. D. Papadopoulos, private communication.